New insights into the role of AGNs in forming the cluster red sequence

Rhythm Shimakawa [1,2]★ Jose Manuel Pérez-Martínez [3,4,5] Yusei Koyama,[6] Masayuki Tanaka,[7] Ichi Tanaka,[6] Tadayuki Kodama,[3] Nina A. Hatch [8] Huub J. A. Röttgering,[9] Helmut Dannerbauer[4,5] and Jaron D. Kurk[10]

[1]*Waseda Institute for Advanced Study (WIAS), Waseda University, 1-21-1 Nishi-Waseda, Shinjuku, Tokyo 169-0051, Japan*
[2]*Center for Data Science, Waseda University, 1-6-1 Nishi-Waseda, Shinjuku, Tokyo 169-0051, Japan*
[3]*Astronomical Institute, Tohoku University, 6-3 Aramaki, Aoba, Sendai, Miyagi 980-8578, Japan*
[4]*Instituto de Astrofísica de Canarias, E-38205 La Laguna, Tenerife, Spain*
[5]*Departamento de Astrofísica, Universidad de la Laguna, E-38206 La Laguna, Tenerife, Spain*
[6]*Subaru Telescope, National Astronomical Observatory of Japan, National Institutes of Natural Sciences, 650 North A'ohoku Place, Hilo, HI 96720, USA*
[7]*National Astronomical Observatory of Japan (NAOJ), National Institutes of Natural Sciences, 2-21-1 Osawa, Mitaka, Tokyo 181-8588, Japan*
[8]*School of Physics and Astronomy, University of Nottingham, University Park, Nottingham NG7 2RD, UK*
[9]*Leiden Observatory, Leiden University, PO Box 9513, NL-2300 RA Leiden, the Netherlands*
[10]*Max-Planck-Institut für Extraterrestrische Physik, Giessenbachstraße 1, D-85748 Garching, Germany*

ABSTRACT

As a considerable investment of time from various telescope facilities was dedicated toward studying the Spiderweb protocluster at $z = 2.2$, it so far remains one of the most extensively studied protocluster. We report here the latest results in this field, adding a new dimension to previous research on cluster formation at high redshift. Previous studies have reported a significant overdensity ($\delta \sim 10$) of massive Hα (+ [N II])-emitting galaxies in 3700 comoving Mpc^3. Many of these were previously considered to be dusty, actively star-forming galaxies, given their rest-frame optical and infrared features. However, this study argues that a third of them are more likely to be 'passively evolving' galaxies with low-luminosity active galactic nuclei (AGNs) rather than star-forming galaxies, given the multiwavelength spectral energy distribution (SED) fitting including an AGN component. For their SED-based star formation rates to be valid, bulk of their Hα + [N II] emission should come from the central AGNs. This difference in interpretation between this work and past studies, including ours, is particularly supported by the recent deep *Chandra*/X-ray observation. Furthermore, we have spectroscopically confirmed a quiescent nature for one of these AGNs, with its multiple stellar absorption lines but also low-ionization emission lines. This important update provides new insights into the role of AGNs in forming the cluster red sequence observed in the present-day universe.

Key words: galaxies: clusters: individual: PKS 1138−262 – galaxies: evolution – galaxies: formation – galaxies: high-redshift.

1 INTRODUCTION

Galaxy protoclusters at $z = 2$–3 are ideal sites for monitoring the transitions from young forming galaxy clusters to evolved clusters in the universe, and the role of the physical drivers in the formation of the tight cluster red sequence thereafter (Bower, Lucey & Ellis 1992; Kodama et al. 2007; Cai et al. 2016; Darvish et al. 2016; Mei et al. 2023). During this transition phase, a wide range of physics is involved not only in the protocluster galaxies but also in the surrounding intergalactic medium (IGM), such as cold streams flowing into hot massive haloes, metal-enriched gas recycling, and pre-heating by energetic feedback (Dekel et al. 2009; Valentino et al. 2016; Arrigoni Battaia et al. 2018; Umehata et al. 2019; Daddi et al. 2021, 2022; Kooistra et al. 2022; Dong et al. 2023; Zhang et al. 2023).

Negative (and positive) feedback from active galactic nuclei (AGNs), known as AGN feedback, is thought to be a key mechanism regulating the formation of massive galaxies, particularly at high redshift, and thus the red sequence of clusters (e.g. Best et al. 2005; Springel, Di Matteo & Hernquist 2005; Croton et al. 2006; Hopkins et al. 2006; Schawinski et al. 2007, 2014; Somerville et al. 2008; Kaviraj et al. 2011; Alexander & Hickox 2012; Fabian 2012; Harrison et al. 2012; Costa, Sijacki & Haehnelt 2014; Genzel et al. 2014; Shimizu et al. 2015; Harrison 2017; Le Fèvre et al. 2019; Terrazas et al. 2020; Piotrowska et al. 2022; Bluck et al. 2023a; Bluck, Piotrowska & Maiolino 2023b; Byrne et al. 2023; Wellons et al. 2023). Galaxy–galaxy interactions are expected to be enhanced in high-z protocluster environments (Okamoto & Habe 2000; Gottlöber, Klypin & Kravtsov 2001; Hine et al. 2016; Liu et al. 2023), which may trigger AGN activity and hence AGN feedback (Lehmer et al. 2009, 2013; Krishnan et al. 2017; Vito et al. 2020; Polletta et al. 2021; Monson et al. 2023). Although it is quite challenging to obtain a straightforward proof of AGN feedback in the star formation

★ E-mail: rhythm.shimakawa@aoni.waseda.jp

quenching, the AGN activity has been detected in quiescent galaxies at high redshifts in recent deep observations (Kriek et al. 2009; Olsen et al. 2013; Marsan et al. 2015; Man et al. 2016; Gobat et al. 2017; Ito et al. 2022; Kubo et al. 2022; Carnall et al. 2023), providing the role of the AGN activity in the star formation quenching.

In this context, the Spiderweb protocluster, consisting of the radio galaxy, PKS 1138−262 at $z = 2.16$ (Bolton, Savage & Wright 1979; Roettgering et al. 1994, 1997; van Ojik 1995), and its associated galaxies, is the representative 'maturing' protocluster system that forms a salient red sequence (Kodama et al. 2007; Zirm et al. 2008; Doherty et al. 2010; Tanaka et al. 2010, 2013). This system has been intensively studied for years by diverse communities. The Spiderweb protocluster is the first protocluster at $z > 2$ that was specifically targeted and confirmed by Kurk et al. (2000) and Pentericci et al. (2000), on the basis of its large rotation measures of the polarized radio emission (Carilli et al. 1997; Pentericci et al. 1997, see also Anderson et al. 2022). The signal of the thermal Sunyaev–Zeldovich effect has now been detected, suggesting that it is a dynamically active system with $M_{500} = 3.46 \times 10^{13}$ M$_\odot$, before becoming a bona fide cluster seen in the local universe (Di Mascolo et al. 2023, see also Tozzi et al. 2022b). Following the initial confirmation of the overdensity traced by Lyα emitting galaxies (Kurk et al. 2000; Venemans et al. 2007), significant overdensities of different populations have been repeatedly observed at multiple wavelengths, such as Hα emitting galaxies (Kurk et al. 2004a; Hatch et al. 2011; Koyama et al. 2013a; Shimakawa et al. 2018), red-sequence galaxies (Kodama et al. 2007; Zirm et al. 2008; Doherty et al. 2010; Tanaka et al. 2010, 2013), dust-obscured objects (Mayo et al. 2012; Koyama et al. 2013b; Valtchanov et al. 2013; Dannerbauer et al. 2014; Zeballos et al. 2018), X-ray sources (Carilli et al. 2002; Pentericci et al. 2002; Tozzi et al. 2022a), and CO(1–0) emitters (Jin et al. 2021; Chen et al. 2024, see also Emonts et al. 2018; Tadaki et al. 2019). Besides, the kinetic structure of the protocluster system has also been studied through spectroscopic campaigns for associated cluster members (Pentericci et al. 2000; Kurk et al. 2004b; Croft et al. 2005; Shimakawa et al. 2014, 2015; Jin et al. 2021; Pérez-Martínez et al. 2023).

Based on the available multiband data, previous studies have reported more abundant red massive Hα emitters (HAEs) with stellar masses $M_\star \gtrsim 1 \times 10^{11}$ M$_\odot$ in the Spiderweb protocluster (Hatch et al. 2011; Koyama et al. 2013a, b; Shimakawa et al. 2018). These red HAEs were considered to be dusty starbursts before they became bright red-sequence galaxies, as seen in the local galaxy clusters. In fact, they, including the Spiderweb radio galaxy, tend to have irregular and clumpy morphologies in the rest-frame ultraviolet images (Koyama et al. 2013a, see also Stevens et al. 2003; Miley et al. 2006; Hatch et al. 2008), suggesting that their star formation would be driven by merger events. However, we need to consider the influence of AGNs on the characterization of these massive HAEs. Although we knew this was an important issue (Shimakawa et al. 2018; Pérez-Martínez et al. 2023), we had overlooked it in our previous work. Moreover, the recent extremely deep X-ray observation with *Chandra*/Advanced CCD Imaging Spectrometer-S array (ACIS-S; Tozzi et al. 2022a) has detected more AGN members, and we now have 14 X-ray counterparts out of 30 massive HAEs with $M_\star > 2 \times 10^{10}$ M$_\odot$ in the updated stellar mass estimation (see Section 3.2), which increases the severity of the issue.

Therefore, this study focuses on the characterization of 14 massive HAEs (Shimakawa et al. 2018) with X-ray counterparts (Tozzi et al. 2022a) in the Spiderweb protocluster at $z = 2.16$, using multiwavelength data sets collected from previous studies. We are primarily interested to revisit their stellar masses and star forma-
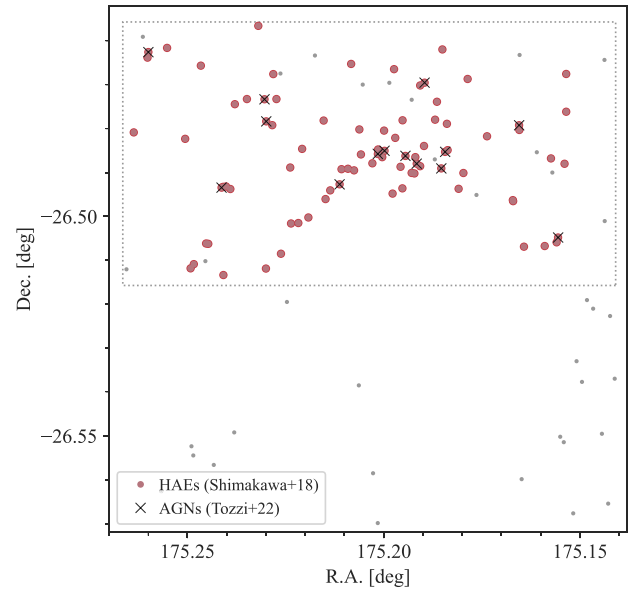

Figure 1. Sky distribution of HAEs (Koyama et al. 2013a) and X-ray counterparts (Tozzi et al. 2022a), which are, respectively, shown by the circle and cross symbols. The red filled circles represent the HAE samples in this paper, which are located within the MAHALO-Deep Field (Shimakawa et al. 2018), as indicated by the dotted rectangular area.

tion rates (SFRs) in view of AGN contributions. We also include complementary Very Large Telescope (VLT)/K-band Multi Object Spectrograph (KMOS; Pérez-Martínez et al. 2023) and Keck/Multi Object Spectrometer For InfraRed Exploration (MOSFIRE) data to validate our conclusions. In conjunction with the spectral energy distribution (SED) fitting code used in this work (Yang et al. 2020), we assume a flat Lambda cold dark matter model with $h = 0.693$ and $\Omega_{\mathrm{M}} = 0.286$; these values are consistent with those obtained from the 9-year *Wilkinson Microwave Anisotropy Probe* (*WMAP*) data (Hinshaw et al. 2013). We use the Chabrier (2003) stellar initial mass function (IMF) and the AB magnitude system (Oke & Gunn 1983). Values for Galactic extinction and dust reddening are, respectively, based on the Fitzpatrick (1999) extinction curve and Schlafly & Finkbeiner (2011). When we refer to the figures and tables included in this paper, we use capitalized words (e.g. Fig. 1 or Table 1), thereby making them easily distinguishable from those in the literature (e.g. fig. 1 or table 1).

2 DATA AND METHODOLOGY

The main focus of this paper is to constrain the stellar masses and SFRs of 14 X-ray AGNs associated with the Spiderweb protocluster at $z = 2.16$ (Tozzi et al. 2022a, table 5) with the *Chandra X-ray Observatory* (Weisskopf et al. 2000). All these have been confirmed in our previous work through Hα (+ [N II]) narrow-band imaging (Shimakawa et al. 2018) with the Multi-Object InfraRed Camera and Spectrograph (MOIRCS) on the Subaru Telescope (Ichikawa et al. 2006; Suzuki et al. 2008). We then discuss the role of AGNs in the formation of the red sequence in protoclusters. We first used 84 HAEs in the Spiderweb protocluster (Fig. 1), 14 out of which were confirmed as X-ray AGNs (hereafter referred to as X-ray HAEs) by Tozzi et al. (2022a). These 84 HAE sources are originally based on 97 narrow-band samples, selected down to the limiting flux of 3×10^{-17} erg s^{-1} cm^{-2} (Shimakawa et al. 2018, table 2), but with some updates from recent spectroscopic

Table 1. Catalogue of the X-ray HAEs. Column (1): ID numbers in Shimakawa et al. (2018); column (2): ID members in Tozzi et al. (2022a); columns (3) and (4): coordinates; column (5): latest spectroscopic redshifts; column (6): reference lines of spec-z; column (7): reference papers; column (8): stellar masses; column (9): SFRs; column (10): AGN fractions; and column (11): AGN type (Sy1 or Sy2) from the X-CIGALE code (Yang et al. 2020). Intrinsic properties of ID = 73 (the Spiderweb radio galaxy) may deviate from our measurements as we do not consider the radio component in the SED fitting and also due to its complicated morphology. ID = 77 has no spec-z but is confirmed as Lyα emitter. Sky coordinates, spectroscopic redshifts, stellar masses, and SFRs for all 84 HAE members, including those without X-ray counterparts, are available in Table A1.

ID (1)	ID_X (2)	RA (3)	Dec. (4)	z (5)	Line (6)	Reference (latest) (7)	$M_\star$ (10^{10} $M_\odot$) (8)	SFR ($M_\star$ yr^{-1}) (9)	f_{AGN} (10)	Type (11)
14	57	11:40:37.34	−26:30:17.3	2.1684	Hα	Pérez-Martínez et al. (2023)	19.52 ± 6.70	6.92 ± 4.67	0.20 ± 0.02	Sy1
28	90	11:40:50.70	−26:29:33.6	2.1532	CO	Jin et al. (2021)	7.61 ± 3.29	4.82 ± 4.70	0.37 ± 0.19	Sy1
29	34	11:40:57.91	−26:29:36.3	2.1703	Hα	Pérez-Martínez et al. (2023)	7.46 ± 5.65	6.18 ± 4.79	0.50 ± 0.18	Sy1
40	86	11:40:44.48	−26:29:20.6	2.1620	Lyα	Croft et al. (2005)	9.19 ± 2.00	5.33 ± 3.43	0.52 ± 0.22	Sy2
46	75	11:40:45.98	−26:29:16.7	2.1557	Hα	Pérez-Martínez et al. (2023)	2.10 ± 3.24	7.87 ± 7.66	0.89 ± 0.07	Sy1
48	87	11:40:46.67	−26:29:10.3	2.1663	Hα	Pérez-Martínez et al. (2023)	18.32 ± 2.16	3.53 ± 0.45	0.31 ± 0.04	Sy1
55	74	11:40:44.25	−26:29:07.0	2.1583	H&K	This work (Section 4.3)	23.23 ± 2.92	2.54 ± 1.23	0.40 ± 0.21	Sy1
58	7	11:40:47.95	−26:29:06.1	2.1568	Hα	Pérez-Martínez et al. (2023)	6.79 ± 1.13	41.34 ± 15.57	0.75 ± 0.08	Sy2
68	36	11:40:39.73	−26:28:45.2	2.1620	Lyα	Croft et al. (2005)	14.72 ± 4.13	35.88 ± 30.98	0.39 ± 0.17	Sy1
71	12	11:40:55.18	−26:28:42.0	2.1630	Hα	Pérez-Martínez et al. (2023)	3.25 ± 1.12	3.27 ± 3.20	0.51 ± 0.14	Sy1
73	58	11:40:48.36	−26:29:08.7	2.1618	CO	Jin et al. (2021)	261.7 ± 39.4	542.4 ± 81.1	0.60 ± 0.03	Sy2
77	9	11:40:55.29	−26:28:23.8	–	Lyα	Kurk et al. (2000)	3.22 ± 1.42	5.73 ± 4.23	0.19 ± 0.19	Sy1
83	73	11:40:45.50	−26:28:10.2	–	–		2.42 ± 1.11	5.85 ± 6.14	0.40 ± 0.27	Sy1
95	80	11:41:02.39	−26:27:45.1	2.1510	Hα	Pérez-Martínez et al. (2023)	12.78 ± 16.37	65.23 ± 29.66	0.62 ± 0.04	Sy2

observations (Jin et al. 2021; Pérez-Martínez et al. 2023). Among the 84 HAEs, 49 HAEs are identified spectroscopically and the remaining are validated by the BzK_s colour selection (Daddi et al. 2004, 2005) to exclude foreground and background emitters (see Section 2.1.3 and Shimakawa et al. 2018 for details). Considering previous identifications of ∼40 protocluster members that do not overlap with HAEs (e.g. Pentericci et al. 2000; Tanaka et al. 2013; Jin et al. 2021), our HAE sample represents approximately 70 per cent of the entire protocluster members confirmed to date. For the X-ray HAEs, 13 out of 14 sources have spec-z confirmations reported in literature (Pentericci et al. 2000; Kurk et al. 2004b; Croft et al. 2005; Tanaka et al. 2013; Shimakawa et al. 2014; Jin et al. 2021; Pérez-Martínez et al. 2023). The detailed information of these X-ray HAEs can be found in Table 1.

2.1 Data

To perform the SED fitting using the X-CIGALE (version 2022.1; Yang et al. 2020) for the HAE sample, we have collected as much multiband photometry data as possible from the archive data and literature (Kurk et al. 2000; Miley et al. 2006; Kodama et al. 2007; Seymour et al. 2007; Koyama et al. 2013a; Valtchanov et al. 2013; Dannerbauer et al. 2014; Shimakawa et al. 2018), as details are summarized in Table 2. Overall, their photometric flux densities and errors were taken from our previous measurements (Shimakawa 2017; Shimakawa et al. 2018), which are based on the forced MAG_AUTO photometry using the narrow-band (NB2071) image for source detection with the SEXTRACTOR (version 2.19.5; Bertin & Arnouts 1996). Flux errors were independently measured by the deviations in randomly positioned empty apertures, with corresponding in size to the Kron radii in each photometry to take into account the pixel-to-pixel correlation (see Shimakawa 2017; Shimakawa et al. 2018 for more details).

2.1.1 Chandra X-ray Observatory

We have adopted the *Chandra* ACIS-S photometry in the soft (0.5–2.0 keV) and hard (2–10 keV) bands reported by Tozzi et al. (2022a).

Table 2. Photometric data sets used in this work (see references listed in the fifth column for more details). One should note here that we show the most relevant reference to each data in this work, part of which were independently reduced and analysed across multiple papers.

Telescope/ Instrument	Band	λ (μm)	Depth (3σ)	Reference
Chandra/				
ACIS-S	Hard (2–10 keV)		34.6	Tozzi et al. (2022a)
	Soft (0.5–2 keV)		34.0	...
VLT/				
VIMOS	U	0.37	27.1	–
FORS2	B	0.43	26.8	Kurk et al. (2000)
FORS2	R	0.65	26.2	...
FORS2	I	0.79	26.4	...
HAWK-I	Y	1.02	26.1	Dannerbauer et al. (2014)
HAWK-I	H	1.62	25.1	...
HAWK-I	K_s	2.15	24.8	...
Subaru/				
S-Cam	B	0.44	26.6	Shimakawa et al. (2018)
	z'	0.91	26.4	Koyama et al. (2013a)
MOIRCS	J	1.25	24.3	Kodama et al. (2007)
	K_s	2.15	24.0	Shimakawa et al. (2018)
	NB	2.07	24.0	...
HST/				
ACS	*F475W*	0.47	26.3	Miley et al. (2006)
	F814W	0.81	27.0	...
Spitzer/				
IRAC	ch1	3.56	21.4	Seymour et al. (2007)
	ch2	4.50	21.6	...
MIPS	24 μm	23.6	19.9	Koyama et al. (2013a)
Herschel/				
PACS	Green	100	4.5 mJy	Seymour et al. (2012)
	Red	160	9.0 mJy	...
SPIRE	PSW	250	7.5 mJy	Valtchanov et al. (2013)
	PMW	350	8.0 mJy	...
	PLW	500	9.0 mJy	...
APEX/				
LABOCA		870	4.5 mJy	Dannerbauer et al. (2014)

The extremely deep exposure ($\sim$700 ks) reaches the flux limits of 1.3×10^{-16} and 3.9×10^{-16} erg s^{-1} cm^{-2} in the soft and hard bands, respectively, which allowed them to obtain a total of 107 X-ray sources in the range of 2.5 Mpc from the Spiderweb radio galaxy. Among them, 14 sources have optical counterparts confirmed as HAEs within $\sim$1 arcsec (Shimakawa et al. 2018), including the Spiderweb galaxy itself (Fig. 1). For running the X-CIGALE SED fitting code (Yang et al. 2020), in this study, their unabsorbed luminosity and errors in the soft and hard bands and photon indexes (Γ) were taken from table 5 in Tozzi et al. (2022a). After transforming the K-corrected luminosity to those in the observed frame with $k(z) = (1 + z)^{\Gamma - 2}$, they were converted to unabsorbed flux densities using the flux converter implemented in the X-CIGALE SED fitting code. We should note that we were forced to adopt observed fluxes and errors for ID = 29 and 40 (Table 1), which have been reported as Compton-thick candidates in Tozzi et al. (2022a).

2.1.2 Very Large Telescope

The B-band data taken from Very Large Telescope (VLT)/FOcal Reducer and low dispersion Spectrograph 1 (FORS1) and the r- and i-band data from VLT/FOcal Reducer and low dispersion Spectrograph 2 (FORS2) were distributed by Kurk et al. (2000, 2004a) via private communication in Koyama et al. (2013a). The target region is also covered by the deep near-infrared (YHK_s) imaging with VLT/High Acuity Wide-field K-band Imager (HAWK-I; Dannerbauer et al. 2017). Photometric measurements for these bands have already been conducted in our previous work (Shimakawa 2017; Shimakawa et al. 2018), and thus, we simply adopted the flux densities and errors derived in them. Furthermore, in this work, we have used deep U-band data with VLT/VIsible Multi Object Spectrograph (VIMOS) from the ESO Science Archive (programme ID 383.A-0891). The U-band photometry was performed in the same way as in Shimakawa et al. (2018), which obtained the forced measurements using the narrow-band (NB2071) image with Subaru/MOIRCS as the reference image. The point source limiting magnitudes for these data sets are summarized in Table 2.

2.1.3 Subaru Telescope

In addition to the VLT data, the optical (Bz') and near-infrared (JK_s and NB2071) data were obtained with the Suprime-Cam and MOIRCS on the Subaru Telescope, respectively, as a part of the long-running campaign for galaxy clusters and protoclusters at high redshifts, termed the Mapping H-Alpha and Lines of Oxygen with Subaru (MAHALO-Subaru; see also Kodama et al. 2007; Tanaka et al. 2011; Koyama et al. 2013a; Shimakawa et al. 2018). We employed the same forced measurements in these bands as in Shimakawa et al. (2018). The MOIRCS NB2071 filter, with a central wavelength of 2.071 µm and full width at half-maximum (FWHM) = 270 Å, is capable of capturing strong emission lines such as the Hα line at $z = 2.155 \pm 0.020$ and the [O III] λ5008 line at $z = 3.135 \pm 0.026$.

Based on these data, the narrow-band selection (K_s–NB2071) and the $Bz'K_s$ colour–colour diagram were conducted for the HAE selection at $z = 2.16$, as described in more detail by Shimakawa et al. (2018). The narrow-band selection in our previous work detected 97 narrow-band emitters above the 3σ confidence level, of which 36, 32, and 13 emitters were further selected as spec-z (or dual Lyα and Hα) members, $Bz'K_s$ colour-selected members, and member candidates that could not be rejected by the colours,

respectively. The remaining 16 narrow-band emitters were defined as foreground or background emitters. The expected contamination rate for the 13 member candidates is $\sim$10 per cent, given the follow-up spectroscopy (Shimakawa et al. 2018). Subsequently, the number of spec-z confirmations was increased to $N = 49$ by the Australia Telescope Compact Array (ATCA) CO(1–0) observation (Jin et al. 2021) and the VLT/KMOS K-band spectroscopy (Pérez-Martínez et al. 2023). As a result, we now have 49, 23, and 12 HAEs with spec-z confirmations, colour validations, and candidates, respectively; hence, a total of 84 (= 49 + 23 + 12) protocluster members of HAEs in this paper. However, it should be noted that this paper solely focuses on 14 X-ray HAEs and the remaining 70 non-X-ray HAEs are used only as a reference sample but summarized in Appendix A and Table A1.

2.1.4 Hubble Space Telescope

We have included the *Hubble Space Telescope* (*HST*)/Advanced Camera for Surveys (ACS; *F475W* and *F814W*) data from the *Hubble* Legacy Archive. The *HST*/ACS data were first used by Stevens et al. (2003) and have been studied repeatedly in several papers (Miley et al. 2006; Hatch et al. 2008; Koyama et al. 2013a; Naufal et al. 2023). In this work, we do not use the original high-resolution images, but adopt the point spread function (PSF)-convolved forced measurements of Shimakawa et al. (2018). The obtained flux densities are consistent with those in the similar bands from the ground-based telescopes, as seen in Section 3.1.

2.1.5 Spitzer Space Telescope

In addition, we used the *Spitzer*/InfraRed Array Camera (IRAC) 3.6 µm (ch1) and 4.5 µm (ch2) bands from the NASA/IPAC Infrared Science Archive (see also Seymour et al. 2007), which cover 92 per cent of the HAE sample (or $\sim$80 per cent of the survey area, Fig. 1), and 13 out of 14 X-ray HAEs in this work (only missing ID = 95 in the ch1 band, Table 1). As described in Shimakawa et al. (2018), we used the post-Basic Calibrated Data (PBCD) products from the *Spitzer* data archive library. However, we modified the IRAC photometry from the literature based on the forced measurements on the narrow-band (NB2071) image, as for the other photometric bands, instead of the independent measurements performed in the previous work. Here, we obtained a fixed aperture photometry with a diameter of 4 arcsec, and then performed the aperture corrections by multiplying by 1.20 and 1.22 in the ch1 and ch2 bands, respectively. This revision somehow helps us constrain the stellar masses of the X-ray HAEs and the upper limits for the lower mass HAEs.

We also adopted the *Spitzer*/Multiband Imaging Photometer for *Spitzer* (MIPS) 24 µm source photometry based on the reduced data provided by Koyama et al. (2013a, see also Mayo et al. 2012). As in the case of the IRAC photometric estimates, we remeasured flux densities using fixed aperture photometry, but with a diameter of 7 arcsec, and then applied the aperture correction by multiplying by a factor of 2.8. Because of the large seeing size (6 arcsec), we overestimated the MIPS flux densities in some cases that the targets have close neighbours. However, we stress that the addition of MIPS photometry does not make a significant difference to our conclusions.

2.1.6 Far-infrared and submillimetre data

Furthermore, we made the best possible effort to constrain the upper limits of SFRs by including public source photometry and

limiting fluxes from Dannerbauer et al. (2017, table 2), which are based on far-infrared to submillimetre (submm) observations with the *Herschel Space Telescope* and the Atacama Pathfinder Experiment (APEX). However, the current shallow far-infrared and submm data show slight effect on the SED fitting results. We have used flux densities and errors in the *Herschel*/Photodetector Array Camera and Spectrometer (PACS) 100 and 160 μm bands (Seymour et al. 2012), *Herschel*/Spectral and Photometric Imaging REceiver (SPIRE) 250, 350, and 500 μm bands (Valtchanov et al. 2013), and APEX/Large APEX BOlometer CAmera (LABOCA) 870 μm band for the HAEs with submm counterparts (Dannerbauer et al. 2017), and the 3σ limits to constrain the upper limits for the remaining HAEs (Table 2). For the 14 X-ray HAEs, only two of the most massive systems (ID = 73 and 95), including the Spiderweb radio galaxy, are reliably detected by Dannerbauer et al. (2017, DKB07 and DKB16).

In addition, we adopted the recent 870 μm flux measurement in the Atacama Large Millimeter/submillimeter Array (ALMA) Band 7 for four X-ray HAEs (ID = 14, 46, 48, and 71 in Table 1), where the details of the data processing and photometry are explained by Koyama et al. (in preparation). We confirmed that the ALMA Band 7 data have only a small impact on the derivation of their stellar masses and SFRs in the SED fitting and hence do not affect the conclusions of this paper as in the case of the other infrared and submm data.

2.2 SED modelling

In order to obtain physical quantities for AGN host galaxies, it is very important to perform a SED fitting taking into account the AGN component. We therefore ran the SED fitting code, X-CIGALE (version 2022.1; Boquien et al. 2019; Yang et al. 2020, 2022), to characterize the X-ray HAEs, including the other HAEs for reference. The X-CIGALE is excellent for the X-ray AGNs like our targets, as it not only covers the ultraviolet to radio regimes but also has an X-ray module. The photometric fluxes and errors in the multiwavelength bands were taken from our previous measurements (Shimakawa 2017; Shimakawa et al. 2018), as described in the last subsection.

For the SED fitting, this paper generally follows the module selection in the original paper (Yang et al. 2020). Specifically, we used the stellar templates of Bruzual & Charlot (2003) with a fixed stellar metallicity of $Z = 0.004$ ($0.2\ Z_\odot$) and the Chabrier (2003) IMF, assuming a delayed exponentially declining star formation history (SFH) $\propto t \exp(-t/\tau)$. We refer to Pearson et al. (2017) for the selection of stellar population models in the SFH: the values of t and τ are allowed to be age_main = [0.5, 1, 2, 3] Gyr and tau_main = [0.1, 0.3, 0.5, 1, 3, 5] Gyr in the main stellar populations and age_burst = [0.001, 0.01, 0.03, 0.1, 0.2] Gyr and tau_burst = 10^6 Gyr in the late burst, respectively. Here, the late burst with $\tau = 10^6$ Gyr approximates constant star formation. The mass fraction of the late burst is allowed to be [0.001, 0.01, 0.1, 0.2]. The selection of stellar populations in the SFH is most critical for the derivation of stellar masses and SFRs, and moderately produces the systematic difference. Particularly, stellar masses (SFRs) of some young, low-mass HAEs, which are beyond the scope of this paper, may be overestimated (underestimated) (Appendix A). However, it should be noted that this does not change the obtained trends and hence the main conclusion of this paper. An additional explanation of the coherence of the stellar mass estimation between this work and the previous study (Shimakawa et al. 2018) is provided in Appendix A.

The model fit also includes nebular templates with an ionization parameter ($\log U = -2$) and $Z_{gas} = 0.02$ based on Inoue (2011) computed from the CLOUDY 0.8.00 photoionization code (Ferland et al. 2017). We have adopted the Calzetti et al. (2000) attenuation

Table 3. Fitting parameters of AGN and X-ray models adopted by this work in the X-CIGALE code (Yang et al. 2020).

Module/ Parameter	Values
SKIRTOR2016/	
Torus optical depth at 9.7 μm	7
Torus density radial parameter	1
Torus density angular parameter	1
Angle between the equatorial plan and edge of the torus	40
Ratio of the max to min radii of the torus	20
Viewing angle	30, 70
AGN fraction in total infrared luminosity	0.01–0.99
Extinction law of polar dust	SMC
$E(B-V)$ of polar dust	0.01–1
Temperature of polar dust	100
Emissivity of polar dust	1.6
XRAY/	
AGN photon index	1.8
Max deviation from $\alpha_{ox}-L_{2500}$ relation	0.2
LMXB photon index	1.56
HMXB photon index	2.0

law with $E(B-V) = 0.01$–1.0 mag and dust emission from Draine et al. (2014) without changing the default model parameters. In addition, the SED models include AGN components with AGN fractions $f_{AGN} = 0.01$–0.99, which is defined by the fraction of AGN infrared luminosity to the total infrared luminosity (Yang et al. 2020). X-ray emissivity and AGN models are based on Stalevski et al. (2016), where we selected the same model parameters (Table 3) as in Yang et al. (2020, table 3) except for $E(B-V)$, which is allowed to be 0.01–1.0 mag by considering high column densities of some X-ray HAEs (Tozzi et al. 2022a, and see also Section 4.2). It should be noted that the model selection adopted here may not be the best choice for our sample, and these parameters have rather been selected as a compromise because of the limited data availability (see also Section 3.1). We also include the effect of IGM absorption based on Meiksin (2006). Consequently, a total of 15 396 480 models per redshift were adopted to conduct the SED fitting for the X-ray HAEs. It took about 1 h to run the SED fitting in the environment of 28 × 3.3 GHz Intel CPU.

3 RESULTS

3.1 Result of SED fitting

The best-fitting SEDs of the X-ray HAE samples are shown in Fig. 2, indicating that the SED fitting worked well with the best reduced chi-squares $\chi_\nu^2 < 5$, except for the two X-ray HAEs (ID = 48 and 83 with $\chi_\nu^2 = 5$–10). The derived stellar masses, SFRs, AGN fractions, and AGN types and their associated errors are summarized in Table 1. Overall, the SED fitting with the AGN components and the X-ray modules help to decrease the reduced chi-squares by a factor of 1.5 on average, and makes the host galaxy spectra redder owing to AGN contributions in the rest-frame ultraviolet. For example, the median contribution at $\lambda_{rest} = 2800$ Å is as much as 48 per cent, while it is only approximately 18 per cent in the rest-frame optical band ($\lambda_{rest} = 6500$ Å). In the most cases, host galaxy components are more dominant than AGNs in the rest-frame optical, except for two X-ray HAEs (ID = 29 and 46, Fig. 2). On the other hand, obtained AGN fractions in the infrared luminosity (f_{AGN}) exceed 50 per cent in six X-ray HAEs (Table 1). Particularly, the best-fitting stellar mass
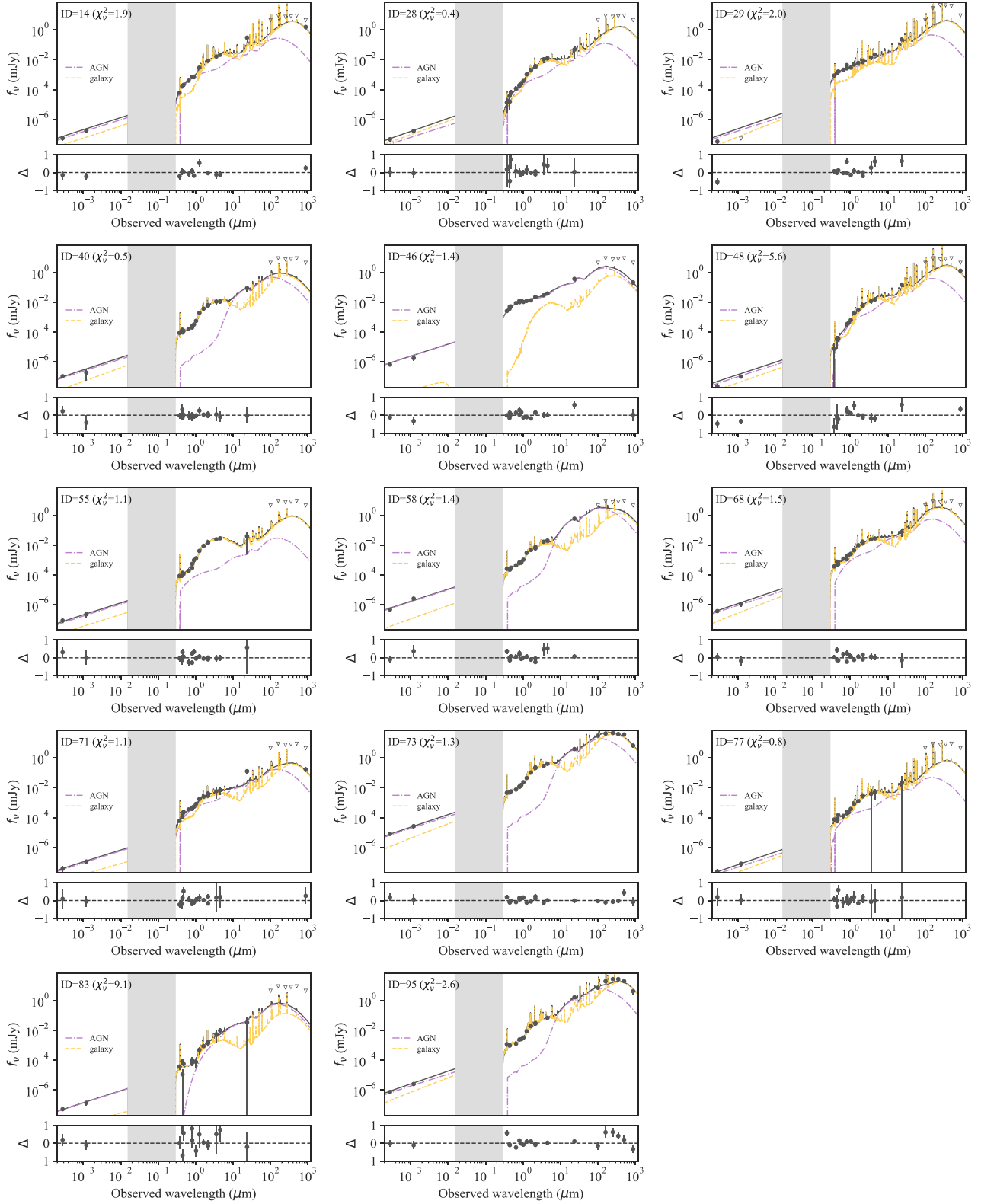
Figure 2. The best-fitting SED spectra (black lines on the upper panels) and normalized residual errors Δ (black circles on the lower panels) of the X-ray HAEs obtained by the X-CIGALE code. The relative flux residuals Δ are defined by $\Delta \equiv (f_{\nu,\text{in}} - f_{\nu,\text{out}})/f_{\nu,\text{out}}$, where $f_{\nu,\text{in}}$ and $f_{\nu,\text{out}}$ are observed flux densities and the best-fitting flux densities in the broad-bands, respectively. The identification number and the best-fitting reduced chi-squares are denoted at upper left in each panel. The filled black circles show observed flux densities in the filter bands for each target, while the opened inverted triangles are the upper limits adopted for non-detection in the infrared and/or submm bands (see Sections 2.1.5 and 2.1.6). The magenta and yellow lines on the upper panels depict AGN and galaxy components, respectively. We conveniently masked an unused wavelength range from the rest-frame 5 nm (corresponding to the limit of the X-ray module) to the Lyman limit by the grey regions (see Section 3.1).

of one of the X-ray HAEs (ID = 46) significantly decreases by a factor of 3.5 due to a high AGN fraction of $f_{AGN} = 0.89$ when the AGN component is included. However, we note that it largely depends on the SED modelling. It should be noted that there may be larger uncertainties beyond the inferred values in the Spiderweb radio galaxy (ID = 73) owing to its extended and complex morphology. In addition, we have confirmed that SED-based SFRs of non-X-ray HAEs are self-consistent with their Hα-based SFRs based on the narrow-band fluxes of Shimakawa et al. (2018), as shown in Appendix A.

Fig. 2 also suggests that the best-fitting SEDs broadly agree with the X-ray observation in the most cases; however, there is still room for improvement. Whereas, determining more complex parameters with a limited sample size and only the two X-ray bands is difficult and may need investigations from a more fundamental aspect, which is beyond of the scope of this paper. In addition, the number of the SED models in this work (15 396 480 per redshift) is close to the cache size in our system environment. Detailed analyses of local relics of high-redshift AGNs will be helpful to optimize the parameter selection and to gain a more precise understanding of characteristics of such X-ray HAEs at $z > 2$. Besides, one should note that the X-CIGALE covers a wavelength range up to the rest-frame 5 nm in the X-ray module (Yang et al. 2020) and its IGM absorption model does not consider the Lyman limit systems. However, our photometric data do not cover the rest-frame 5 nm to the Lyman limit, and thus these issues do not affect our SED fitting results practically (Fig. 2).

As mentioned in Section 2.1, we confirmed that there is no significant impact on observational trends (see Section 3.2) even without infrared and submm data at $\lambda > 20$ µm. Nevertheless, it can be seen that their flux densities and the upper limits are broadly consistent with the best-fitting SEDs (Fig. 2). There are significant flux excesses in the MIPS 24 µm band in some cases, which seem to be caused by blending issue, given the limited seeing size at FWHM of 6 arcsec. The *JWST* Mid-InfraRed Instrument (MIRI; Rieke et al. 2015) will be able to provide more reliable photometry and spectra with much better spatial resolution (FWHM ~ 0.8 arcsec) in the similar infrared bands. Additionally, combined high-resolution data from the upcoming *JWST*/Near-InfraRed Camera (NIRCam) run (Dannerbauer et al. 2021) and the existing *HST*/ACS data (Miley et al. 2006) may help to achieve the galaxy–AGN decomposition in a more immediate manner, especially for the X-ray HAEs with high AGN fractions (e.g. see Ding, Silverman & Onoue 2022).

3.2 Star-forming main sequence

It is well known that there is a tight relationship between SFRs and stellar masses of galaxies termed star-forming main sequence (Brinchmann et al. 2004; Daddi et al. 2007; Elbaz et al. 2007; Noeske et al. 2007; Salim et al. 2007; Whitaker et al. 2012; Speagle et al. 2014; Lee et al. 2015; Renzini & Peng 2015; Tacchella et al. 2016; Tomczak et al. 2016; Förster Schreiber & Wuyts 2020; Popesso et al. 2023). The resulting SFRs and stellar masses are represented in Fig. 3, indicating that 10 out of 30 massive HAEs with $M_\star > 2 \times 10^{10}$ M$_\odot$ are located significantly (~ 1 dex) below the star-forming main sequence formed by non-X-ray HAEs (e.g. Popesso et al. 2023), despite of the detection of Hα + [N II] line emissions. Most of them (9/10) are HAEs with low X-ray luminosity ($L_X < 4 \times 10^{43}$ erg s^{-1} in the hard band), where one of the X-ray HAEs (ID = 46) with low SFR has not been counted due to its substantial margin of error in the stellar mass. Fig. 3 also indicates approximately half of massive HAEs with $M_\star > 2 \times 10^{10}$ M$_\odot$ host X-ray AGNs ($\sim 14/30$), which yields the AGN fraction of 0.42 ± 0.03 when including three additional

quiescent galaxies with spectroscopic identifications (Tanaka et al. 2013).

We show how the addition of the AGN templates ($f_{AGN} \geq 0.01$) and the X-ray module affects their stellar mass and SFR measurements, as shown in the right panel of Fig. 3. It can be seen that the addition of the AGN components has a significant effect on quiescent properties of the X-ray HAEs, except for the two X-ray HAEs (ID = 40 and 55) that remain quiescent irrespective of the AGN models. On the other hand, most of massive star-forming HAEs without X-ray counterparts in Tozzi et al. (2022a) are significantly shifted from the star-forming main sequence to the passive sequence, assuming that they have AGN components with an AGN fraction of $f_{AGN} \geq 0.01$. Here, their X-ray flux densities are constrained by the upper limits (Table 2) but multiplied by 1.5 for the soft band taking account of typical X-ray absorption in the X-ray HAEs. The result suggests that the recent deep *Chandra* X-ray observation (Tozzi et al. 2022a) plays a rather important role in updating the SFR measurements of these X-ray HAEs, as well as in revealing such intriguing properties of AGN host galaxies in the Spiderweb protocluster.

With regard to the non-X-ray HAEs, we observe only one non-X-ray HAE (1/10) lying well below the star-forming main sequence (ID = 89 in Shimakawa et al. 2018) regardless of whether we assume that they host AGNs with the AGN fraction $f_{AGN} > 0.01$ or not (Fig. 3). The HAE ID = 89 could be a dusty [O III] emitter at $z \sim 3.1$ or [O II] emitter at $z = 4.6$, given no clear detection in the *UBr* bands. We also note that the most massive non-X-ray HAE (ID = 54) would be an AGN according to the Baldwin–Phillips–Terlevich (BPT) diagram (Shimakawa et al. 2015; Pérez-Martínez et al. 2023), which further supports the very high AGN fraction in the Spiderweb protocluster.

Importantly, as noted in Section 2.2, we cannot completely deny the possibility that the obtained trend could be model dependent, although we confirmed that the trend itself does not change even if we chose different model settings with best efforts. Direct evidence is highly desirable to ensure star formation quenching in these AGN host galaxies. At present, there is no sufficient observational constraint to determine the nature of passive evolution for the entire X-ray HAE sample, although we show a spectroscopic identification of the star formation quenching for one of the X-ray HAEs (ID = 55) in Section 4.3.

4 DISCUSSION

4.1 Protocluster versus field

We found that a third of 30 massive HAEs with $M_\star > 2 \times 10^{10}$ M$_\odot$ in the Spiderweb protocluster at $z = 2.16$ have unexpectedly low SFRs, despite their high Hα + [N II] fluxes $> 4 \times 10^{-17}$ erg s^{-1} cm^{-2} (Shimakawa et al. 2018). Because the less active HAEs host low-luminosity AGNs ($L_X \lesssim 4 \times 10^{43}$ erg s^{-1}) detected by the recent deep *Chandra* X-ray observation (Tozzi et al. 2022a), the bulk of their Hα (+ [N II]) emission would be driven by AGNs rather than star formation (see also Section 4.2). Our result suggests that the formation process of the red-sequence galaxies is well underway in the Spiderweb protocluster faster than previously thought (Koyama et al. 2013a; Shimakawa et al. 2018). Considering recent identifications of an intracluster medium (ICM) with the deep X-ray and submm observations (Tozzi et al. 2022b; Di Mascolo et al. 2023), the state of the Spiderweb protocluster seems to be very close to the bona fide clusters observed at $z \lesssim 2$. In this context, some passive AGNs in the protocluster centre might have contributed to pre-heating of protocluster ICM (Kooistra et al. 2022; Dong et al. 2023),
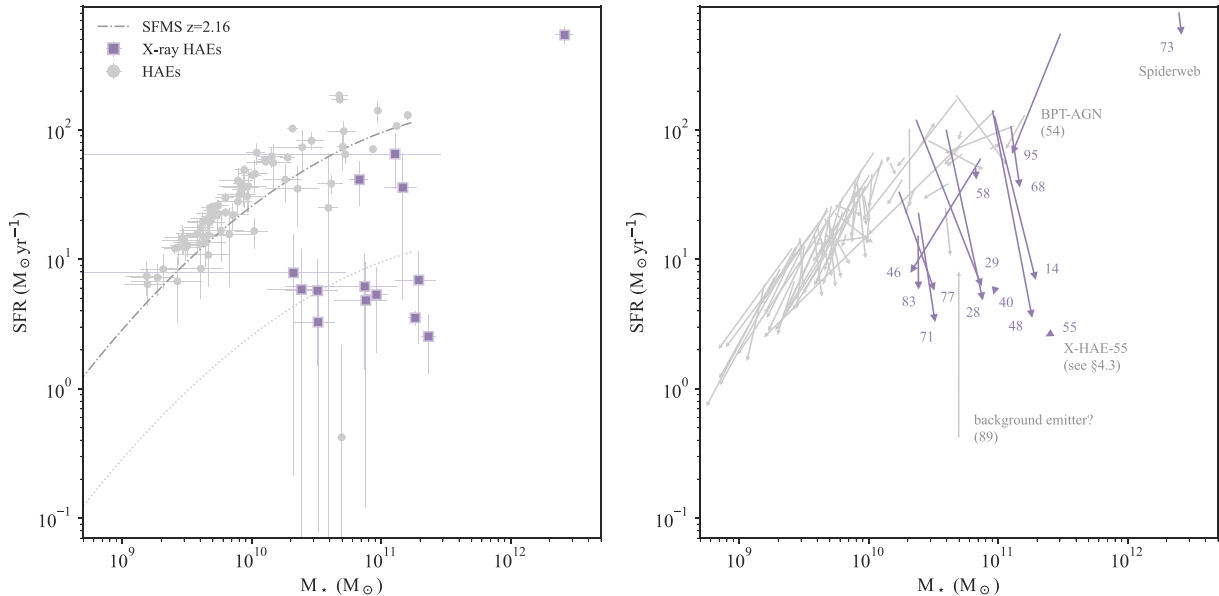
Figure 3. The left panel shows SED-based SFRs versus stellar masses ($M_\star$) of 84 HAEs in the Spiderweb protocluster at $z = 2.2$ (Shimakawa et al. 2018). The purple and grey symbols represent HAEs with ($N = 14$) and without ($N = 70$) X-ray counterparts (Tozzi et al. 2022a), respectively. We here do not consider the AGN components in the SED fitting for the latter case. The black dot–dash curve represents the star-forming main sequence at $z = 2.16$ from Popesso et al. (2023) with the IMF correction from Kroupa (2001) to Chabrier (2003), and its $\times 0.1$ relation is depicted by the grey dotted curve. On the right panel, arrow symbols depict how these values change on the SFR–$M_\star$ plane when assuming the AGN components with AGN fractions $f_{AGN} \geq 0.01$ in the SED fitting (see text), each of which is attached with the identification number in Table 1. Additional comments are included in the figure for the sake of clarity.

although high-resolution IGM tomography is required to test the pre-heating scenario in greater detail. Additionally, the result suggests that AGNs may be involved in their star formation quenching. However, it is premature to get to the conclusion at this point, without identifying physical associations between AGNs and host galaxies. The remainder of this subsection discusses whether such an intriguing result is a peculiar trend in high-density environments or more ubiquitous throughout the universe at high redshifts.

To discuss the environmental dependence, we used the X-ray-selected AGNs at $z \sim 2$ in the Cosmological Evolution Survey (COS-MOS) field (Scoville et al. 2007) and the Great Observatories Origins Deep Survey-South (GOODS-S) field (Giavalisco et al. 2004), which are based on the *Chandra*-COSMOS Legacy Survey (Civano et al. 2016) and the COSMOS2020 catalogue (Weaver et al. 2022), and the *Chandra Deep Field*-South Survey (Liu et al. 2017; Luo et al. 2017) and the 3D-HST catalogue (Skelton et al. 2014), respectively. In the COSMOS field, a total of 51 sources with spectroscopic redshifts of $z = 1.5$–2.5 over ~ 2.2 deg^2 are selected from Suh et al. (2020) with X-ray fluxes, down to 3.7×10^{-16} erg s^{-1} cm^{-2} in the soft band and 1.5×10^{-15} erg s^{-1} cm^{-2} in the hard band. They are respectively higher than the flux limits of 1.3×10^{-16} and 3.9×10^{-16} erg s^{-1} cm^{-2} in the Spiderweb protocluster (Tozzi et al. 2022a). Therefore, a clear sampling bias can be noted in the sense that we are missing X-ray faint AGNs in the COSMOS field. Specifically, we adopted source photometry in the CFHT Large Area *U*-band Deep Survey (CLAUDS) *U* band (Sawicki et al. 2019), *grizy* bands from the Hyper Suprime-Cam Subaru Strategic Program (HSC-SSP) Public Data Release 2 (PDR2; Aihara et al. 2018, 2019), *BgVrizz'* and several medium bands from the Subaru Suprime-Cam data (Taniguchi et al. 2007, 2015), *YJHK*$_s$ bands from the UltraVISTA Data Release 4 (DR4; McCracken et al. 2012), and IRAC ch1 and ch2 data from the *Spitzer* Extended Deep Survey (SEDS; Ashby et al. 2013, 2018).

Meanwhile, we employed 57 X-ray-selected AGNs at z_{spec} = 1.5–2.5 in the GOODS-S field (~ 0.05 deg^2) down to 6.4×10^{-18} erg s^{-1} cm^{-2} in the soft band and 2.7×10^{-17} erg s^{-1} cm^{-2} in the hard band (Liu et al. 2017; Luo et al. 2017), which are significantly deeper than those in the Spiderweb protocluster (see also fig. 4 in Tozzi et al. 2022a). It should be noted here that we used their unabsorbed X-ray luminosity only in the hard band and photon indexes for the SED fitting due to the data availability in Liu et al. (2017). Photometric data were taken from the 3D-HST catalogue (Skelton et al. 2014), which is a collection of VLT/VIMOS *UR* bands from Nonino et al. (2009), *UBVR*$_c$*I* bands from the Garching–Bonn Deep Survey (Erben et al. 2005; Hilde-brandt et al. 2006), median bands from the Multiwavelength Survey by Yale-Chile (MUSYC; Cardamone et al. 2010), *HST*/ACS *F*435*W*, *F*606*W* bands data from GOODS (Giavalisco et al. 2004), *F*606*W*, *F*814*W*, *F*125*W*, *F*160*W* bands from the Cosmic Assembly Near-infrared Deep Extragalactic Legacy Survey (CANDELS; Grogin et al. 2011; Koekemoer et al. 2011), *F*140*W* band from 3D-HST (Brammer et al. 2012), *JHK*$_s$ bands from GOODS and FIREWORKS (Wuyts et al. 2008; Retzlaff et al. 2010), *JK*$_s$ bands from Taiwan ECDFS Near-Infrared Survey (TENIS; Hsieh et al. 2012), and IRAC ch1 and ch2 data from SEDS (Ashby et al. 2013). We then performed the SED fitting in the exact same manner as for the HAE sample (see Section 2.2). For a relatively fair comparison, we employed the band photometry in the X-ray and the *U*-to-4.5 μm bands for these field samples.

Fig. 4 shows the resultant comparison plot between the Spiderweb protocluster and the COSMOS and GOODS-S fields on the SFR–$M_\star$ plane. Despite the use of similar data and the SED modelling, the figure indicates a clear difference. Specifically, X-ray HAEs in the Spiderweb protocluster are preferentially located below the star-forming main sequence compared to those in the COSMOS field at
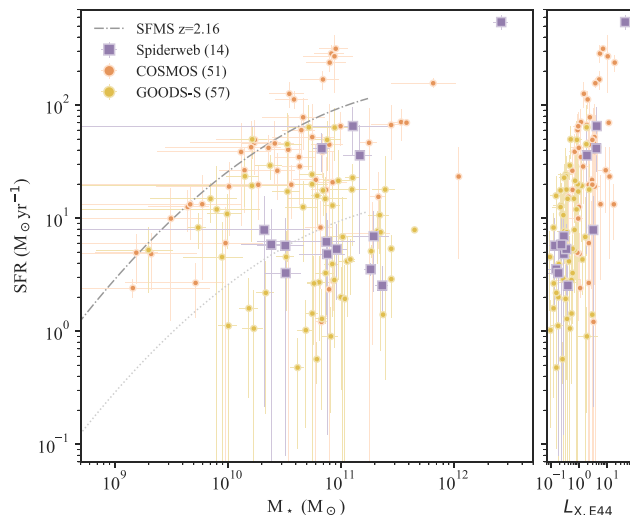
Figure 4. The left panel is the same as Fig. 3 but for 14 X-ray HAEs in the Spiderweb protocluster (purple squares) and 51 and 57 X-ray AGNs at z = 1.5–2.5 in the COSMOS and GODDS-S fields, respectively (orange and yellow circles). The right panel shows SFRs versus X-ray luminosity in the hard band (2–10 keV) in the unit of 1×10^{44} erg s^{-1} for the same samples as in the left panel.

Figure 5. SED-based SFRs (SFR$_{SED}$) versus Hα-based SFRs without dust correction (SFR$_{H\alpha,obs}$) of 14 X-ray HAEs. Their SFR$_{H\alpha}$ values are simply converted through the Kennicutt (1998) prescription based on observed narrow-band fluxes, assuming 30 per cent contributions of [N II] lines. The solid, dot–dash, and dashed lines, respectively, assume 100, 50, and 10 per cent contributions of star formation to their observed Hα fluxes, although the assumed fractions should be minimum, given dust attenuation.

z = 1.5–2.5, while they show a better agreement with the GOODS-S samples at z = 1.5–2.5. The lack of X-ray AGNs with low specific SFRs (sSFRs) in the COSMOS field is likely due to the sampling bias, such as a different X-ray flux limit and a different spectroscopic identification method, rather than the environmental dependence. X-ray AGNs with low sSFRs in the Spiderweb protocluster tend to have lower X-ray luminosity just below the flux limit in the COSMOS field (Fig. 4). Ito et al. (2022) have detected faint AGN emissions in the composite X-ray image of quiescent galaxies in the same COSMOS field at a similar redshift, which further supports this scenario. Their composite X-ray flux in the soft band is $\sim 3 \times 10^{-17}$ erg s^{-1} cm^{-2} in passive galaxies with $M_\star = 1 \times 10^{11}$ M$_\odot$ at z = 2.0–2.5 (Ito et al., private communication). It is thus reasonable to consider that we are simply missing such passively evolving galaxies with faint X-ray emissions in the COSMOS field. In addition, the sampling bias of redshift identifications may affect the comparison analysis. While the X-ray AGNs in the protocluster have been selected based on Hα + [N II] lines with near-infrared observations, those in the COSMOS field have been originally selected based on the optical spectroscopy with Keck/DEep Imaging Multi-Object Spectrograp (DEIMOS; Hasinger et al. 2018). This difference in sample selection may lead the apparent difference between the Spiderweb protocluster and the COSMOS field, as shown in Fig. 4.

Indeed, we also observed quiescent hosts with low-luminosity AGNs in the GOODS-S field, where the X-ray flux limit is much deeper than those in the COSMOS field and the Spiderweb protocluster (Fig. 4). However, we should note that there is no tight correlation between SFRs and X-ray luminosity within the range of $< 1 \times 10^{44}$ erg s^{-1}, suggesting that instantaneous AGN activity is not connected with star formation quenching in massive galaxies (see also discussion in Terrazas et al. 2020; Piotrowska et al. 2022; Ward et al. 2022; Bluck et al. 2023a, b). Taken together, we conclude that the discovery of passive HAEs with low-luminosity AGNs in the Spiderweb protocluster would not be caused environmental effects. Such objects can be found even in the general field as long as one has very deep X-ray data, and rather, they may be more abundant
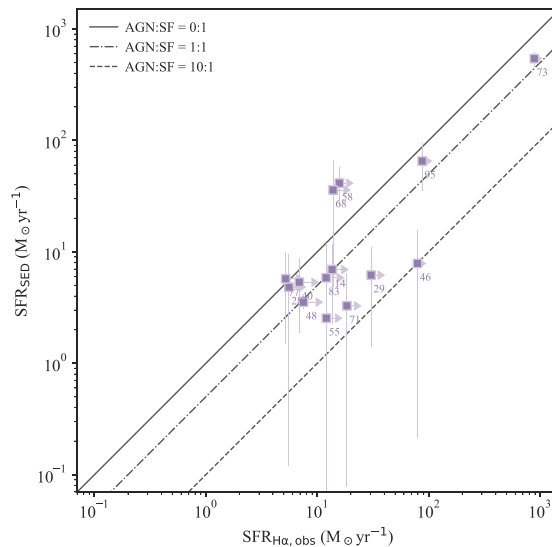
than we previously thought. On the other hand, the Spiderweb protocluster may yet have a high fraction of such passive HAEs with low-luminosity AGNs since high-density environments can provoke galaxy mergers hence promote the mass growth of black holes (Okamoto & Habe 2000; Gottlöber et al. 2001; Hine et al. 2016). To this end, a homogeneous and deep observation in both Hα and X-ray will be required for deriving the abundance of star-forming and passive galaxies with X-ray AGNs down to the low X-ray luminosity in a quantitative manner.

4.2 Impacts of AGNs on Hα emission

We have argued so far that 9 out of 14 X-ray HAEs seem to be post-star-forming galaxies despite the presence of Hα (+ [N II]) line emissions (>4×10^{-17} erg s^{-1} cm^{-2}; Shimakawa et al. 2018). In this subsection, we discuss how large AGN contributions make up for their Hα fluxes detected by the narrow-band imaging.

Comparing two independently obtained SFRs from the SED fitting and observed Hα fluxes is a convenient way to examine the AGN contribution (Fig. 5). In the latter case we estimated Hα-based SFRs (SFR$_{H\alpha,obs}$) using the Kennicutt (1998) prescription with additional scaling factor of 0.59 to convert to the Chabrier (2003) IMF. We adopted Hα fluxes of X-ray HAEs from their narrow-band fluxes obtained by Shimakawa et al. (2018), assuming 30 per cent of [N II] flux contribution to the narrow-band fluxes. It should be noted that we do not take dust extinction into account for the sake of simplicity, i.e. the Hα-based SFR assumed here should be minimum. For reference, we expect that typical Hα extinctions of these massive galaxies with $M_\star \sim 1 \times 10^{11}$ M$_\odot$ would be ~ 2 mag if they were normal star-forming galaxies (Shimakawa et al. 2015), which increase their SFRs by a factor of 6.31 when applying dust correction. Fig. 5 shows that a majority of the X-ray HAEs require AGN contributions to their Hα + [N II] lines for making them consistent with their SED-based SFRs. Particularly, at least one of those should be affected by approximately 90 per cent or more even if dust correction is
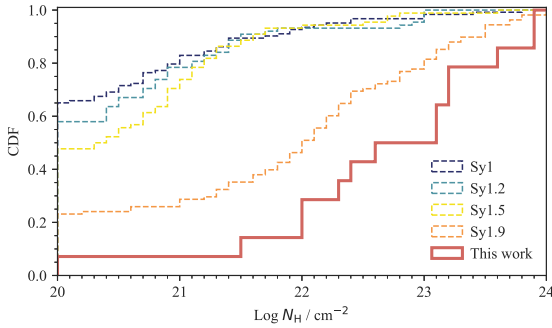
Figure 6. The red thick line shows the normalized cumulative distribution function of H I column densities for the 14 X-ray HAEs from Tozzi et al. (2022a). We here assumed $N_H = 10^{24}$ cm^{-2} for two Compton-thick AGNs and $N_H = 10^{20}$ cm^{-2} for one AGN with $N_H = 0$ cm^{-2} in the literature for the sake of visibility. We also adopted the upper limits ($N_H \sim 3 \times 10^{22}$ cm^{-2}) for three AGNs (see Tozzi et al. 2022a, table 5). Additionally, for reference, the column densities of various types of Seyfert AGNs at $z < 0.4$ are shown by dashed lines (Mejía-Restrepo et al. 2022), where Seyfert 1, 1.2, 1.5, and 1.9 sources are coloured blue, cyan, yellow, and orange, respectively.

not taken into account. We thus conclude that the bulk of Hα emission detected in the previous narrow-band imaging (Shimakawa et al. 2018) would originate from AGNs and not host galaxies. A follow-up deep near-infrared spectroscopy will be helpful to further constrain their emission line contributions as discussed in Section 4.3. The forthcoming Paβ imaging with *JWST*/NIRCam (Dannerbauer et al. 2021) could be also able to spatially decompose emission-line contributions from AGNs and host galaxies.

Dust attenuation reduces observed Hα fluxes from not only star-forming regions but also AGNs. Tozzi et al. (2022a) reported that X-ray HAEs in the Spiderweb protocluster tend to have high H I column densities, which suggests that their Hα fluxes (and perhaps FWHM) would be significantly suppressed as observed in type 1.9 AGNs at lower redshifts (Mejía-Restrepo et al. 2022; Ricci et al. 2022). Fig. 6 presents normalized cumulative distribution functions (CDFs) of the H I column densities for the X-ray HAEs and X-ray selected AGNs at $z < 0.4$ from the BAT AGN Spectroscopic Survey/Data Release 2 (BASS/DR2). We have collected the column density values of the X-ray HAEs from Tozzi et al. (2022a, table 5) and those at low redshifts from a compilation by Ricci et al. (2017), Oh et al. (2018), and Mejía-Restrepo et al. (2022). Although we have to treat comparison results in the figure with caution, given the potential sampling bias, H I column densities are greater than 1×10^{22} cm^{-2} for a majority of the X-ray HAEs, which is more similar to those of Seyfert 1.9 AGNs than those of Seyfert <1.9. This suggests that familiar broad-line emissions such as Mg II and Hβ would not be visible in the X-ray HAE sample, and even Hα broad lines may be suppressed. Such a trend also agrees with the recent findings that high-redshift AGNs tend to be dust obscured by their massive host galaxies (Gilli et al. 2022; Silverman et al. 2023).

In fact, Pérez-Martínez et al. (2023) obtained Hα spectra for 8 out 14 X-ray HAEs with the VLT/KMOS (Sharples et al. 2013), including ID = 14, 28, 29, 46, 55, 58, 71, and 95 in Table 1, but only two of them (ID = 46 and 95) show relatively broad components with >700 km s^{-1}. We tentatively estimated their black hole masses (M_{BH}) based on the best-fitting Hα broad-line properties from Pérez-Martínez et al. (2023, fig. 3), through the prescription in Mejía-Restrepo et al. (2022, equation 2), which is modified from the Greene
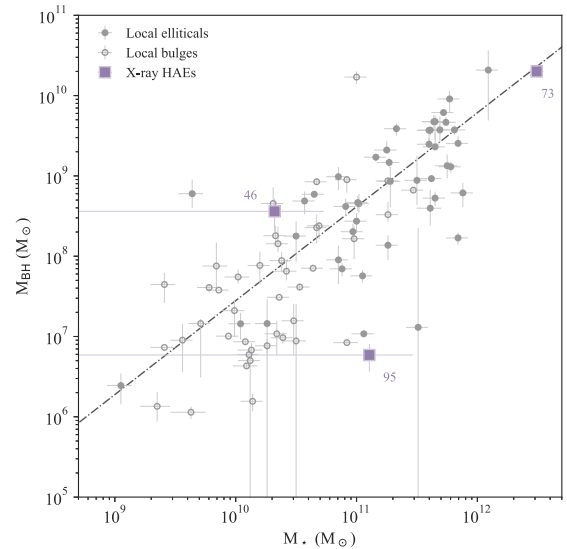

Figure 7. Black hole mass versus stellar mass for local elliptical galaxies (filled circles) and classical and pseudo-bulges (opened circles) from Kormendy & Ho (2013). We here plot the tentative black hole mass measurements for three X-ray HAEs (ID = 46, 73, 95; Table 1) as shown by the magenta squares. Black hole masses of ID = 46 and 95 are newly obtained through the Mejía-Restrepo et al. (2022) prescription, while we adopted the estimation by Tozzi et al. (2022a) for the Spiderweb radio galaxy (ID = 73). The dot–dash line depicts the local M_{BH}–$M_\star$ relation (Kormendy & Ho 2013) scaled by Reines & Volonteri (2015).

& Ho (2005) calibration,

$$M_{BH} = 10^{6.43} \times \left(\frac{L_{H\alpha}}{10^{42} \text{ erg s}^{-1}} \right)^{0.55} \left(\frac{FWHM_{H\alpha}}{10^3 \text{ km s}^{-1}} \right)^{2.06} M_\odot. \quad (1)$$

Obtained black hole masses are $M_{BH} = 3.6 \pm 1.6 \times 10^8$ and $5.9 \pm 2.2 \times 10^6$ M$_\odot$ in ID = 46 and 95, respectively (Fig. 7). Both AGNs approximately follow the M_{BH}–$M_\star$ relation of local elliptical galaxies and classical and pseudo-bulges (Kormendy & Ho 2013; Reines & Volonteri 2015) within the margin of error. As discussed above, these tentative measurements may underestimate their black hole masses because of the dust attenuation. We also confirmed that the Spiderweb galaxy (ID = 73) tracks the local M_{BH}–$M_\star$ relation (Fig. 7) when we adopted $M_{BH} = 2 \times 10^{10}$ M$_\odot$ reported by Tozzi et al. (2022a).

The current dust-reddening issue prevents us from investigating their black hole masses as noted by Mejía-Restrepo et al. (2022) and Ricci et al. (2022). The blending issue with the [N II] doublet and the limited signal-to-noise ratio are additional issues for accurately determining the broad-line components. Under such circumstances, for instance, a spectroscopic observation of Paβ at $\lambda_{obs} = 4.05$ µm broad lines with the *JWST* Near-Infrared Spectrograph (NIRSpec) will be a powerful solution to reliably constrain their dust-obscured black hole masses, where the more luminous Paα line at $\lambda_{obs} = 5.93$ µm is out of the wavelength coverage of *JWST*/NIRSpec. In addition, the forthcoming Paβ narrow-band imaging with the *JWST*/NIRCam (Rieke, Kelly & Horner 2005) on the Spiderweb protocluster may help us spatially resolve dust-obscured line emissions from AGNs and star formation. These prospective follow-up analyses can provide useful insights into the growth history of supermassive black holes within red-sequence galaxies in the present-day galaxy clusters.

4.3 Spectroscopic characterization

Fortunately, we obtained the deep near-infrared spectral data from Keck/MOSFIRE for one of the X-ray HAEs, ID = 55 (hereafter X-HAE-55), with $M_\star = 2.32 \pm 0.29 \times 10^{11}$ M$_\odot$ and SFR $= 2.54 \pm 1.23$ M$_\odot$ yr^{-1} (Table 1). The X-HAE-55 was previously discussed as one of the extremely red objects and hence a quiescent galaxy in the Spiderweb protocluster by Doherty et al. (2010) and Tanaka et al. (2013). Interestingly, Hα +[N II] emission with the flux of 1×10^{-16} erg s^{-1} cm^{-2} has been detected by the narrow-band imaging (Koyama et al. 2013a; Shimakawa et al. 2018), which is confirmed by the recent work with the VLT/KMOS spectroscopy (Pérez-Martínez et al. 2023). This work indicated that the bulk of Hα + [N II] emission should come from the AGN based on the AGN + galaxy SED fitting (see also discussion in Tozzi et al. 2022a). Such a passive galaxy with AGN emission has also been reported at $z = 4.6$ (Carnall et al. 2023). This last subsection provides a complementary analysis on the X-HAE-55 based on the deep spectral data.

The spectrum of X-HAE-55 was obtained in 2015 January 26–27 using Keck/MOSFIRE (McLean et al. 2010, 2012) through the Subaru–Keck time exchange framework. The primary targets were quiescent galaxy candidates and the *J*-band grating was used to cover the wavelength range of $\lambda = 1.17$–1.35 µm, which includes the rest-frame 4000 Å break, with a spectral resolution of $R \sim 3300$. The observing conditions were good with a typical seeing size of about 0.7 arcsec in the *J* band. The standard ABBA nodding was applied along the slit with an exposure time of 120 s at each position. The data were reduced in the standard manner using the MOSFIRE Data Reduction Pipeline (MOSFIRE-DRP; see Steidel et al. 2014 for details). The flux was calibrated against A-type stars observed during the nights. The total integration time was 3 h. In this work, we apply 4-pixel binning along the wavelength to increase the signal-to-noise ratio, and the spectrum is shown in Fig. 8.

We then performed the SED fitting with the BAGPIPES code (version 1.0.2; Carnall et al. 2018, 2019) based on the combined data set of photometry from the *U* to ch1 bands (Section 2.2) and the reduced *J*-band spectrum. The BAGPIPES code relies on the PYTHON module MULTINEST for Bayesian analysis (Buchner et al. 2014; Feroz et al. 2019). We rescaled band photometry to exclude the AGN contribution based on flux ratios of the best-fitting galaxy SED to the AGN component obtained from the X-CIGALE (Fig. 2). The redshift was fixed within the range of $z = 2.150$–2.165 given Ca II H&K absorption lines and tentative detections of the [O II] doublet (Fig. 8). It should be noted that this redshift range falls out of the previous measurement in the literature ($z = 2.1694$; Pérez-Martínez et al. 2023), derived from an apparent Hα line in the *K*-band spectrum with the VLT/KMOS spectroscopy. However, it is turned out that the referenced line should be [N II] λ6585 line not Hα line by comparing with the MOSFIRE *J*-band spectrum (Fig. 8). The Hα line emission cannot be seen in the current KMOS data, meaning that the host galaxy is quenched and even AGN-induced Hα line may be hidden by stellar absorption and/or sky noise. In fact, the obtained [N II] fluxes account only for 62 per cent of the narrow-band flux of 1×10^{-16} erg s^{-1} cm^{-2} taken from Shimakawa et al. (2018), and thus, we should be missing unignorable line contributions from the host galaxy and AGN due to the limited signal-to-noise ratio. Despite the missing components, the line spectrum resembles low-ionization nuclear emission-line regions (LINERs; Heckman 1980) given a high [N II]/Hα ratio ($\gtrsim 1$). Such a LINER-like feature in post-star-forming galaxies with low-luminosity AGN is compatible with the recent AGN quenching scenario suggested from the modern hydrodynamic
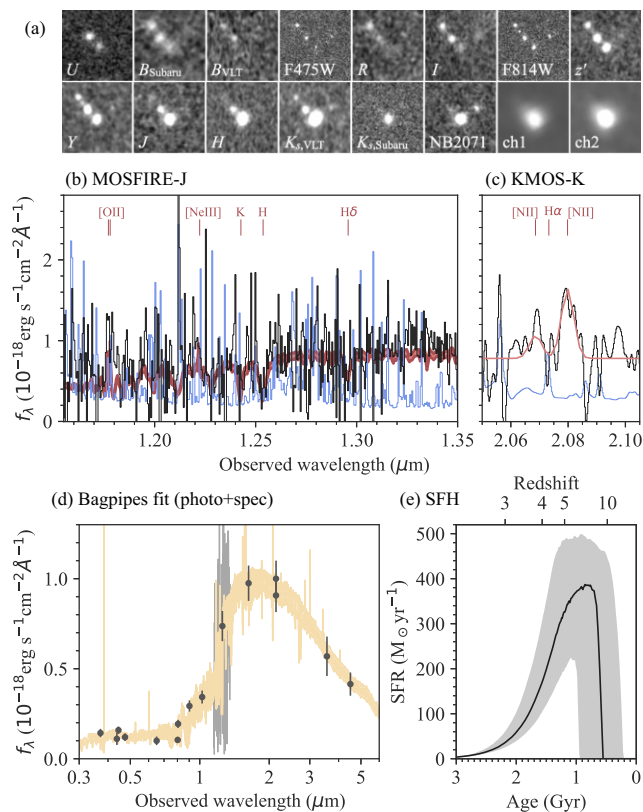

Figure 8. (a) Cut-out images of the X-HAE-55 in the *U* to ch2 bands. (b) The black and blue lines indicate the observed spectrum and noise in the MOSFIRE *J* band, respectively, where the spectrum is binned with 4 spectral pixels. The red filled region depicts the 68 percentile distribution from the BAGPIPES SED fitting. (c) Same as in panel (b) but for the KMOS *K*-band data. The red curve is the best-fitting [N II] $\lambda\lambda$6550, 6585 doublet, assuming the fixed flux ratio of 1:3. The spectrum is convolved by a Gaussian filter with $\sigma = 2$ spectral pixels from the original spectrum in Pérez-Martínez et al. (2023, fig. 3). (d) The orange region indicates the 68 percentile distribution from the best-fitting SED with BAGPIPES (Carnall et al. 2018, 2019), where photometric fluxes and *J*-band spectrum are shown by the black circles with error bars and the grey line, respectively. (e) The best-fitting SFH (black line) and the 68 percentile uncertainty (grey areas) of the X-HAE-55 as a function of the cosmic age and redshift.

cosmological simulations (Terrazas et al. 2020; Piotrowska et al. 2022; Bluck et al. 2023a, b), where cumulative energy injections from kinetic AGN feedback at low Eddington ratios play a pivotal role in star formation quenching. Considering all the factors, the other passive HAEs could also be LINERs, although further investigations must be needed.

The derived best-fitting SED and SFH are summarized in Fig. 8. Because of the similar parameter setting in the SED modelling, obtained stellar mass $= 2.27 \pm 0.25 \times 10^{11}$ M$_\odot$ and SFR $= 4.97 \pm 1.95$ M$_\odot$ yr^{-1} are consistent with those from the X-CIGALE (Table 1). In addition, the best-fitting SED spectrum well reproduces stellar absorption lines of Ca II H&K and Hδ seen in the MOSFIRE *J*-band spectrum. Moreover, the best-fitting SFH with associated errors suggest that the X-HAE-55 was intensively formed during $z = 4$–10 (or age of $\sim$2.0 $\pm$ 0.5 Gyr) like high-z submm galaxies (e.g. Smail, Ivison & Blain 1997; da Cunha et al. 2015; Valentino et al. 2020), and then shifted to the quiescent phase over the last $\sim$1 Gyr before the observed redshift ($z = 2.16$). This formation history is consistent with those reported in previous studies

for extremely red objects in the Spiderweb protocluster (Kodama et al. 2007; Doherty et al. 2010; Tanaka et al. 2013). Because we see a clear AGN sign in this system, AGN feedback is a favourite scenario to explain its star formation quenching (e.g. Alexander & Hickox 2012; Fabian 2012; Harrison 2017 and references therein, but see Terrazas et al. 2020; Piotrowska et al. 2022; Bluck et al. 2023a, b). However, we still lack sufficient proof to conclude that with the current data, which needs to be addressed in the future.

5 CONCLUSIONS

Taking the recent deep *Chandra* X-ray observation (Tozzi et al. 2022a) as its basis and using rich data sets compiled from the various previous studies across the multiwavelength, this work revisited the stellar mass and SFR measurements for 14 AGN-host HAEs in the Spiderweb protocluster at $z = 2.16$ (Shimakawa et al. 2018). Our result of the SED fitting indicates that about half of massive HAEs with $M_\star > 2 \times 10^{10}$ M$_\odot$ host X-ray AGNs (14/30). Further, nine massive HAEs with X-ray counterparts and hence X-ray AGNs tend to show low SFRs significantly below ($\sim$1 dex) the star-forming main sequence traced by the other HAEs. This suggests that the bulk of their Hα (+ [N II]) emissions would originate from AGNs rather than from star formation of host galaxies. Here, the SED fitting algorithm X-CIGALE with the X-ray module (Boquien et al. 2019; Yang et al. 2020) and the deep photometry in the X-ray bands (Tozzi et al. 2022a) played the critical role of reproducing such an intriguing trend. Although a follow-up investigation is still needed to directly confirm their quiescence, our follow-up Keck/MOSFIRE and VLT/KMOS data spectroscopically support the quiescent nature for at least one of these AGN hosts.

In the historical context, the Spiderweb protocluster was first confirmed by overdensities of Lyα and Hα (+ [N II]) emitters (Kurk et al. 2000, 2004a, b; Pentericci et al. 2000). Follow-up (spectro)photometric studies then discovered an apparent red sequence formed by extremely red objects with low SFRs (Kodama et al. 2007; Doherty et al. 2010; Tanaka et al. 2010, 2013). Further intensive surveys found Hα (+ [N II]) and dust emissions from most of these red objects. This led to the understanding that the red galaxies in the protocluster would be dominated by dusty starbursts that are on the verge of becoming bright red-sequence galaxies (Koyama et al. 2013a, b; Dannerbauer et al. 2014; Shimakawa et al. 2018). The results of this study suggest that significant fractions of line emissions in the red massive HAEs actually originate from AGNs not star formation, thereby providing a reasonable agreement on such observational results reported thus far.

The results indicate that a third of massive HAEs with $M_\star > 2 \times 10^{10}$ M$_\odot$ are quiescent galaxies with low-luminosity AGNs (9/30). This implies that AGNs may significantly involve passive galaxies in the Spiderweb protocluster as only three additional quiescent members with spectroscopic redshifts have been reported so far (Tanaka et al. 2013). Such a startling evidence of ubiquitous AGNs in the red sequence in the Spiderweb protocluster suggests that AGNs might be physical drivers of their star formation quenching. Further constraints on star formation and AGN activity, as well as physical interplay between host galaxies and AGNs in the protocluster, remain to be addressed in future studies. Some of these may be partially addressed by the forthcoming Paβ imaging with *JWST*/NIRCam (Dannerbauer et al. 2021) and/or further follow-up observations with such as NIRSpec and MIRI on *JWST*.

DATA AVAILABILITY

This work is based on compilation data of previous studies (Table 2, see also Shimakawa 2017; Shimakawa et al. 2018). Each science-ready data will be shared on reasonable request to the corresponding author. Moreover, all the data used in this work can be obtained through the Subaru Mitaka Okayama Kiso Archive (SMOKA) system, the Keck Observatory Archive, the *Hubble* Legacy Archive, the NASA/IPAC Infrared Science Archive, and the ESO Science Archive Facility.

REFERENCES

Aihara H. et al., 2018, PASJ, 70, S4
Aihara H. et al., 2019, PASJ, 71, 114
Alexander D. M., Hickox R. C., 2012, New Astron. Rev., 56, 93
Anderson C. S., et al., 2022, ApJ, 937, 45
Arrigoni Battaia F., Prochaska J. X., Hennawi J. F., Obreja A., Buck T., Cantalupo S., Dutton A. A., Macciò A. V., 2018, MNRAS, 473, 3907
Ashby M. L. N. et al., 2013, ApJ, 769, 80
Ashby M. L. N. et al., 2018, ApJS, 237, 39
Astropy Collaboration, 2013, A&A, 558, A33
Astropy Collaboration, 2018, AJ, 156, 123
Bertin E., Arnouts S., 1996, A&AS, 117, 393
Best P. N., Kauffmann G., Heckman T. M., Brinchmann J., Charlot S., Ivezić Ž., White S. D. M., 2005, MNRAS, 362, 25
Bluck A. F. L. et al., 2023a, preprint (arXiv:2311.02526)
Bluck A. F. L., Piotrowska J. M., Maiolino R., 2023b, ApJ, 944, 108
Bolton J. G., Savage A., Wright A. E., 1979, Aust. J. Phys. Astrophys. Suppl., 46, 1
Boquien M., Burgarella D., Roehlly Y., Buat V., Ciesla L., Corre D., Inoue A. K., Salas H., 2019, A&A, 622, A103

Bower R. G., Lucey J. R., Ellis R. S., 1992, MNRAS, 254, 601
Brammer G. B. et al., 2012, ApJS, 200, 13
Brinchmann J., Charlot S., White S. D. M., Tremonti C., Kauffmann G., Heckman T., Brinkmann J., 2004, MNRAS, 351, 1151
Bruzual G., Charlot S., 2003, MNRAS, 344, 1000
Buchner J. et al., 2014, A&A, 564, A125
Byrne L. et al., 2023, preprint (arXiv:2310.16086)
Cai Z. et al., 2016, ApJ, 833, 135
Calzetti D., Armus L., Bohlin R. C., Kinney A. L., Koornneef J., Storchi-Bergmann T., 2000, ApJ, 533, 682
Cardamone C. N. et al., 2010, ApJS, 189, 270
Carilli C. L., Röttgering H. J. A., van Ojik R., Miley G. K., van Breugel W. J. M., 1997, ApJS, 109, 1
Carilli C. L., Harris D. E., Pentericci L., Röttgering H. J. A., Miley G. K., Kurk J. D., van Breugel W., 2002, ApJ, 567, 781
Carnall A. C., McLure R. J., Dunlop J. S., Davé R., 2018, MNRAS, 480, 4379
Carnall A. C. et al., 2019, MNRAS, 490, 417
Carnall A. C. et al., 2023, Nature, 619, 716
Chabrier G., 2003, PASP, 115, 763
Chen Z. et al., 2024, MNRAS, 527, 8950
Civano F. et al., 2016, ApJ, 819, 62
Costa T., Sijacki D., Haehnelt M. G., 2014, MNRAS, 444, 2355
Croft S., Kurk J., van Breugel W., Stanford S. A., de Vries W., Pentericci L., Röttgering H., 2005, AJ, 130, 867
Croton D. J. et al., 2006, MNRAS, 365, 11
da Cunha E. et al., 2015, ApJ, 806, 110
Daddi E., Cimatti A., Renzini A., Fontana A., Mignoli M., Pozzetti L., Tozzi P., Zamorani G., 2004, ApJ, 617, 746
Daddi E. et al., 2005, ApJ, 626, 680
Daddi E. et al., 2007, ApJ, 670, 156
Daddi E. et al., 2021, A&A, 649, A78
Daddi E. et al., 2022, ApJ, 926, L21
Dannerbauer H. et al., 2014, A&A, 570, A55
Dannerbauer H. et al., 2017, A&A, 608, A48
Dannerbauer H., Koyama Y., Jin S., Kodama T., Perez Martinez J. M., Shimakawa R., 2021, JWST Proposal. Cycle 1, ID #1572
Darvish B., Mobasher B., Sobral D., Rettura A., Scoville N., Faisst A., Capak P., 2016, ApJ, 825, 113
Dekel A. et al., 2009, Nature, 457, 451
Di Mascolo L. et al., 2023, Nature, 615, 809
Ding X., Silverman J. D., Onoue M., 2022, ApJ, 939, L28
Doherty M. et al., 2010, A&A, 509, A83
Dong C., Lee K.-G., Ata M., Horowitz B., Momose R., 2023, ApJ, 945, L28
Draine B. T. et al., 2014, ApJ, 780, 172
Elbaz D. et al., 2007, A&A, 468, 33
Emonts B. H. C. et al., 2018, MNRAS, 477, L60
Erben T. et al., 2005, Astron. Nachr., 326, 432
Fabian A. C., 2012, ARA&A, 50, 455
Ferland G. J. et al., 2017, Rev. Mex. Astron. Astrofis., 53, 385
Feroz F., Hobson M. P., Cameron E., Pettitt A. N., 2019, Open J. Astrophys., 2, 10
Fitzpatrick E. L., 1999, PASP, 111, 63
Förster Schreiber N. M., Wuyts S., 2020, ARA&A, 58, 661
Genzel R. et al., 2014, ApJ, 796, 7
Giavalisco M. et al., 2004, ApJ, 600, L93
Gilli R. et al., 2022, A&A, 666, A17
Gobat R. et al., 2017, A&A, 599, A95
Gottlöber S., Klypin A., Kravtsov A. V., 2001, ApJ, 546, 223
Greene J. E., Ho L. C., 2005, ApJ, 630, 122
Grogin N. A. et al., 2011, ApJS, 197, 35
Harris C. R. et al., 2020, Nature, 585, 357
Harrison C. M., 2017, Nat. Astron., 1, 0165
Harrison C. M. et al., 2012, MNRAS, 426, 1073
Hasinger G. et al., 2018, ApJ, 858, 77
Hatch N. A., Overzier R. A., Röttgering H. J. A., Kurk J. D., Miley G. K., 2008, MNRAS, 383, 931

Hatch N. A., Kurk J. D., Pentericci L., Venemans B. P., Kuiper E., Miley G. K., Röttgering H. J. A., 2011, MNRAS, 415, 2993
Heckman T. M., 1980, A&A, 87, 152
Hildebrandt H. et al., 2006, A&A, 452, 1121
Hine N. K., Geach J. E., Alexander D. M., Lehmer B. D., Chapman S. C., Matsuda Y., 2016, MNRAS, 455, 2363
Hinshaw G. et al., 2013, ApJS, 208, 19
Hopkins P. F., Hernquist L., Cox T. J., Di Matteo T., Robertson B., Springel V., 2006, ApJS, 163, 1
Hsieh B.-C., Wang W.-H., Hsieh C.-C., Lin L., Yan H., Lim J., Ho P. T. P., 2012, ApJS, 203, 23
Hunter J. D., 2007, Comput. Sci. Eng., 9, 90
Ichikawa T. et al., 2006, in McLean I. S., Iye M., eds, Proc. SPIE Vol. 6269, Ground-based and Airborne Instrumentation for Astronomy. SPIE, Bellingham, p. 626916
Inoue A. K., 2011, MNRAS, 415, 2920
Ito K. et al., 2022, ApJ, 929, 53
Jin S. et al., 2021, A&A, 652, A11
Kaviraj S., Schawinski K., Silk J., Shabala S. S., 2011, MNRAS, 415, 3798
Kennicutt R. C., Jr, 1998, ARA&A, 36, 189
Kodama T., Tanaka I., Kajisawa M., Kurk J., Venemans B., De Breuck C., Vernet J., Lidman C., 2007, MNRAS, 377, 1717
Koekemoer A. M. et al., 2011, ApJS, 197, 36
Kooistra R., Inoue S., Lee K.-G., Cen R., Yoshida N., 2022, ApJ, 927, 53
Kormendy J., Ho L. C., 2013, ARA&A, 51, 511
Koyama Y., Kodama T., Tadaki K.-i., Hayashi M., Tanaka M., Smail I., Tanaka I., Kurk J., 2013a, MNRAS, 428, 1551
Koyama Y. et al., 2013b, MNRAS, 434, 423
Kriek M., van Dokkum P. G., Labbé I., Franx M., Illingworth G. D., Marchesini D., Quadri R. F., 2009, ApJ, 700, 221
Krishnan C. et al., 2017, MNRAS, 470, 2170
Kroupa P., 2001, MNRAS, 322, 231
Kubo M. et al., 2022, ApJ, 935, 89
Kurk J. D. et al., 2000, A&A, 358, L1
Kurk J. D., Pentericci L., Röttgering H. J. A., Miley G. K., 2004a, A&A, 428, 793
Kurk J. D., Pentericci L., Overzier R. A., Röttgering H. J. A., Miley G. K., 2004b, A&A, 428, 817
Lee N. et al., 2015, ApJ, 801, 80
Le Fèvre O. et al., 2019, A&A, 625, A51
Lehmer B. D. et al., 2009, ApJ, 691, 687
Lehmer B. D. et al., 2013, ApJ, 765, 87
Liu T. et al., 2017, ApJS, 232, 8
Liu S. et al., 2023, MNRAS, 523, 2422
Luo B. et al., 2017, ApJS, 228, 2
McCracken H. J. et al., 2012, A&A, 544, A156
McLean I. S. et al., 2010, in McLean I. S., Ramsay S. K., Takami H., eds, Proc. SPIE Vol. 7735, Ground-based and Airborne Instrumentation for Astronomy III. SPIE, Bellingham, p. 77351E
McLean I. S., et al., 2012, in McLean I. S., Ramsay S. K., Takami H., eds, Proc. SPIE Vol. 8446, Ground-based and Airborne Instrumentation for Astronomy IV. SPIE, Bellingham, p. 84460J
Man A. W. S. et al., 2016, ApJ, 820, 11
Marsan Z. C. et al., 2015, ApJ, 801, 133
Mayo J. H., Vernet J., De Breuck C., Galametz A., Seymour N., Stern D., 2012, A&A, 539, A33
Mei S. et al., 2023, A&A, 670, A58
Meiksin A., 2006, MNRAS, 365, 807
Mejía-Restrepo J. E. et al., 2022, ApJS, 261, 5
Miley G. K. et al., 2006, ApJ, 650, L29
Monson E. B. et al., 2023, ApJ, 951, 15
Naufal A., Koyama Y., Shimakawa R., Kodama T., 2023, ApJ, 958, 170
Noeske K. G. et al., 2007, ApJ, 660, L43
Nonino M. et al., 2009, ApJS, 183, 244
Oh K. et al., 2018, ApJS, 235, 4
Okamoto T., Habe A., 2000, PASJ, 52, 457
Oke J. B., Gunn J. E., 1983, ApJ, 266, 713
Olsen K. P., Rasmussen J., Toft S., Zirm A. W., 2013, ApJ, 764, 4

Pearson W. J., Wang L., van der Tak F. F. S., Hurley P. D., Burgarella D., Oliver S. J., 2017, A&A, 603, A102

Pentericci L., Roettgering H. J. A., Miley G. K., Carilli C. L., McCarthy P., 1997, A&A, 326, 580

Pentericci L. et al., 2000, A&A, 361, L25

Pentericci L., Kurk J. D., Carilli C. L., Harris D. E., Miley G. K., Röttgering H. J. A., 2002, A&A, 396, 109

Pérez-Martínez J. M. et al., 2023, MNRAS, 518, 1707

Piotrowska J. M., Bluck A. F. L., Maiolino R., Peng Y., 2022, MNRAS, 512, 1052

Polletta M. et al., 2021, A&A, 654, A121

Popesso P. et al., 2023, MNRAS, 519, 1526

Reback J. et al., 2022, pandas-dev/pandas: Pandas 1.4.3 (v1.4.3). Zenodo (https://doi.org/10.5281/zenodo.6702671)

Reines A. E., Volonteri M., 2015, ApJ, 813, 82

Renzini A., Peng Y.-j., 2015, ApJ, 801, L29

Retzlaff J., Rosati P., Dickinson M., Vandame B., Rité C., Nonino M., Cesarsky C., GOODS Team, 2010, A&A, 511, A50

Ricci F., La Franca F., Onori F., Bianchi S., 2017, A&A, 598, A51

Ricci F. et al., 2022, ApJS, 261, 8

Rieke M. J., Kelly D., Horner S., 2005, in Heaney J. B., Burriesci L. G., eds, Proc. SPIE Vol. 5904, Cryogenic Optical Systems and Instruments XI. SPIE, Bellingham, p. 1

Rieke G. H. et al., 2015, PASP, 127, 584

Roettgering H. J. A., Lacy M., Miley G. K., Chambers K. C., Saunders R., 1994, A&AS, 108, 79

Roettgering H. J. A., van Ojik R., Miley G. K., Chambers K. C., van Breugel W. J. M., de Koff S., 1997, A&A, 326, 505

Salim S. et al., 2007, ApJS, 173, 267

Sawicki M. et al., 2019, MNRAS, 489, 5202

Schawinski K., Thomas D., Sarzi M., Maraston C., Kaviraj S., Joo S.-J., Yi S. K., Silk J., 2007, MNRAS, 382, 1415

Schawinski K. et al., 2014, MNRAS, 440, 889

Schlafly E. F., Finkbeiner D. P., 2011, ApJ, 737, 103

Scoville N. et al., 2007, ApJS, 172, 1

Seymour N. et al., 2007, ApJS, 171, 353

Seymour N. et al., 2012, ApJ, 755, 146

Sharples R. et al., 2013, The Messenger, 151, 21

Shimakawa R., 2017, PhD thesis, Graduate University for Advanced Studies, SOKENDAI, Kanagawa, Japan, https://ci.nii.ac.jp/naid/5000010370 20

Shimakawa R., Kodama T., Tadaki K.-i., Tanaka I., Hayashi M., Koyama Y., 2014, MNRAS, 441, L1

Shimakawa R., Kodama T., Tadaki K.-i., Hayashi M., Koyama Y., Tanaka I., 2015, MNRAS, 448, 666

Shimakawa R. et al., 2018, MNRAS, 481, 5630

Shimizu T. T., Mushotzky R. F., Meléndez M., Koss M., Rosario D. J., 2015, MNRAS, 452, 1841

Silverman J. D. et al., 2023, ApJ, 951, L41

Skelton R. E. et al., 2014, ApJS, 214, 24

Smail I., Ivison R. J., Blain A. W., 1997, ApJ, 490, L5

Somerville R. S., Hopkins P. F., Cox T. J., Robertson B. E., Hernquist L., 2008, MNRAS, 391, 481

Speagle J. S., Steinhardt C. L., Capak P. L., Silverman J. D., 2014, ApJS, 214, 15

Springel V., Di Matteo T., Hernquist L., 2005, ApJ, 620, L79

Stalevski M., Ricci C., Ueda Y., Lira P., Fritz J., Baes M., 2016, MNRAS, 458, 2288

Steidel C. C. et al., 2014, ApJ, 795, 165

Stevens J. A. et al., 2003, Nature, 425, 264

Suh H., Civano F., Trakhtenbrot B., Shankar F., Hasinger G., Sanders D. B., Allevato V., 2020, ApJ, 889, 32

Suzuki R. et al., 2008, PASJ, 60, 1347

Tacchella S., Dekel A., Carollo C. M., Ceverino D., DeGraf C., Lapiner S., Mandelker N., Primack Joel R., 2016, MNRAS, 457, 2790

Tadaki K.-i. et al., 2019, PASJ, 71, 40

Tanaka M., De Breuck C., Venemans B., Kurk J., 2010, A&A, 518, A18

Tanaka I. et al., 2011, PASJ, 63, 415

Tanaka M. et al., 2013, ApJ, 772, 113

Taniguchi Y. et al., 2007, ApJS, 172, 9

Taniguchi Y. et al., 2015, PASJ, 67, 104

Taylor M. B., 2005, in Shopbell P., Britton M., Ebert R., eds, ASP Conf. Ser. Vol. 347, Astronomical Data Analysis Software and Systems XIV. Astron. Soc. Pac., San Francisco, p. 29

Terrazas B. A. et al., 2020, MNRAS, 493, 1888

Tomczak A. R. et al., 2016, ApJ, 817, 118

Tozzi P. et al., 2022a, A&A, 662, A54

Tozzi P. et al., 2022b, A&A, 667, A134

Umehata H. et al., 2019, Science, 366, 97

Valentino F. et al., 2016, ApJ, 829, 53

Valentino F. et al., 2020, ApJ, 889, 93

Valtchanov I. et al., 2013, MNRAS, 436, 2505

van Ojik R., 1995, PhD thesis, Univ. Leiden, the Netherlands

Venemans B. P. et al., 2007, A&A, 461, 823

Vito F. et al., 2020, A&A, 642, A149

Ward S. R., Harrison C. M., Costa T., Mainieri V., 2022, MNRAS, 514, 2936

Weaver J. R. et al., 2022, ApJS, 258, 11

Weisskopf M. C., Tananbaum H. D., Van Speybroeck L. P., O'Dell S. L., 2000, in Truemper J. E., Aschenbach B., eds, Proc. SPIE Vol. 4012, X-Ray Optics, Instruments, and Missions III. SPIE, Bellingham, p. 2

Wellons S. et al., 2023, MNRAS, 520, 5394

Whitaker K. E., van Dokkum P. G., Brammer G., Franx M., 2012, ApJ, 754, L29

Wuyts S., Labbé I., Förster Schreiber N. M., Franx M., Rudnick G., Brammer G. B., van Dokkum P. G., 2008, ApJ, 682, 985

Yang G. et al., 2020, MNRAS, 491, 740

Yang G. et al., 2022, ApJ, 927, 192

Zeballos M. et al., 2018, MNRAS, 479, 4577

Zhang S. et al., 2023, Science, 380, 494

Zirm A. W. et al., 2008, ApJ, 680, 224

APPENDIX A: COMPARISON OF OUR MEASUREMENTS WITH THOSE IN PREVIOUS WORK

Given that our choices of stellar populations in the SFH were different from those in previous work, there were systematic differences in
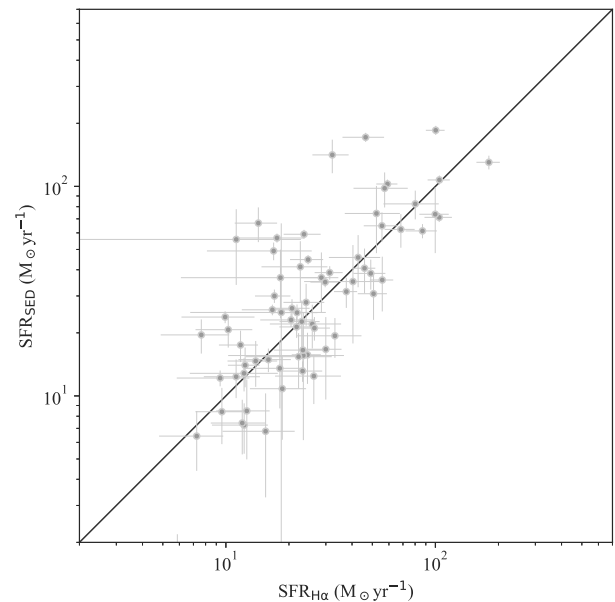

Figure A1. Comparison of SED-based SFRs with Hα-based SFRs for 70 non-X-ray HAEs (grey circles with 1σ error bars) in the Spiderweb protocluster at $z = 2.16$.
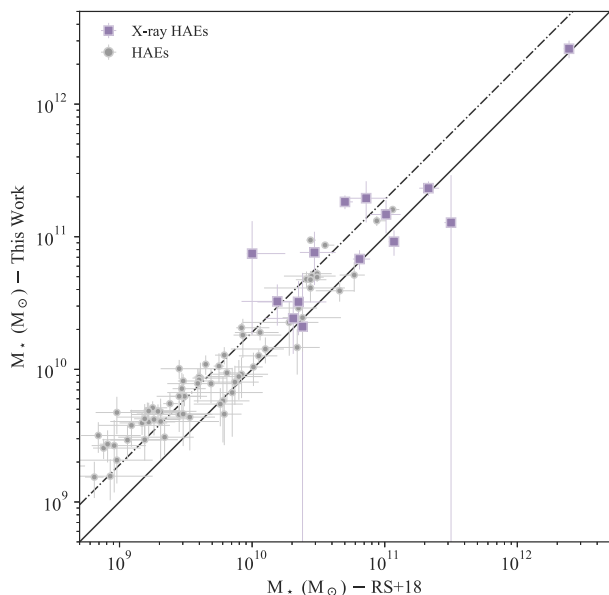
Figure A2. Comparison of the stellar mass estimation between this work and Shimakawa et al. (2018) for the entire 84 HAEs. The black solid and dash–dot lines depict the 1:1 relation and that with an offset of +0.28 dex.

the derivation of physical properties such as stellar masses and SFRs. We then discuss the consistency between SED-based SFRs and Hα-based SFRs of non-X-ray HAEs, and also systematic errors between previous stellar mass measurements of the entire HAEs in Shimakawa et al. (2018) and those in this work.

Fig. A1 shows the comparison between SED-based SFRs and Hα-based SFRs for 70 (= 84 − 14) HAEs (Shimakawa et al. 2018) without the X-ray counterparts (Tozzi et al. 2022a). While their SED-based SFRs are the same as shown in Fig. 2, Hα-based SFRs are derived from narrow-band fluxes in Shimakawa et al. (2018), assuming 30 per cent of flux contributions from the [N II] doublet and dust extinctions from the X-CIGALE SED fitting. We confirmed

that, given the adopted SED modelling, these two different estimates are broadly consistent with each other, although there are deviations from the 1:1 relation.

We then cross-checked our stellar mass measurements with those in the previous work (Shimakawa et al. 2018), which derived the stellar mass based on the FAST SED fitting code (Kriek et al. 2009). The major change in the model assumption compared to previous work is the exclusion of young stellar populations with age ≲100 Myr in the main population; this is because this work set up the model parameters following those in Pearson et al. (2017). The reason for removing the young populations is to derive the reasonable SED-based SFRs for the HAE samples; otherwise, we obtain very high SED-based SFRs that do not match their Hα-based SFRs and the star-forming main sequence at $z = 2.16$ (e.g. Tomczak et al. 2016). This deviation is attributed to the fact that the SED spectra are less sensitive to older stellar populations in general. We should note that such a different model assumption leads to systematic deviations in stellar mass and SFR measurements but does not affect our conclusion as the obtained dependencies of star formation on AGN activities (Figs 3 and 4) do not change.

The extent of deviations in stellar mass measurements between this work and Shimakawa et al. (2018) can be found in Fig. A2. This work tends to obtain higher stellar masses for HAEs with a typical offset value of 0.28 dex, which increases to 0.34 dex when we limit the sample to low-mass HAEs with $M_\star < 1 \times 10^{10}$ M$_\odot$. We also obtained significantly higher stellar masses in some X-ray HAEs by adding the AGN components in the SED fitting. Meanwhile, this work would overestimate stellar masses of some low-mass active HAEs with sSFRs ≳ 10 Gyr^{-1}, meaning their masses could be acquired in the last ≲100 Myr. This is because we do not consider young populations (≤ 100 Myr) as the main stellar population in the SED modelling on the X-CIGALE code (Boquien et al. 2019; Yang et al. 2020), though we include the late constant burst up to 20 per cent in the mass fraction as a compromise. However, it should be noted that this potential issue does not affect the conclusion as these young low-mass HAEs are beyond the scope of this paper.

Table A1. Same as Table 1 but for all 84 HAEs updated by this work. References are written in the following abbreviations (S24: this work; P23: Pérez-Martínez et al. 2023; J21: Jin et al. 2021; S14: Shimakawa et al. 2014; C05: Croft et al. 2005; K04: Kurk et al. 2004b; and K00: Kurk et al. 2000).

ID	RA	Dec.	$z_{\rm spec}$	Line	Reference	$M_\star$ (10^{10} M$_\odot$)	SFR ($M_\star$ yr^{-1})
2	11:40:55.20	−26:30:42.7	2.1447	Hα	P23	0.38 ± 0.12	15.71 ± 4.30
4	11:40:59.81	−26:30:42.6	2.1615	Hα	P23	1.09 ± 0.18	66.79 ± 12.60
5	11:40:57.80	−26:30:48.1	2.1635	Hα	P23	13.19 ± 1.14	107.3 ± 5.4
7	11:40:59.61	−26:30:39.1	2.1645	Hα	P23	2.90 ± 0.69	82.51 ± 12.94
8	11:40:54.28	−26:30:30.6	2.1356	Hα	S14	0.29 ± 0.08	14.67 ± 3.62
9	11:40:38.16	−26:30:24.3	2.1437	Hα	S14	4.11 ± 0.91	38.44 ± 6.27
10	11:40:58.86	−26:30:22.2	–	–	–	0.47 ± 0.15	19.36 ± 4.17
11	11:40:39.43	−26:30:24.8	2.1627	Hα	P23	1.01 ± 0.17	44.74 ± 2.24
12	11:40:37.43	−26:30:21.2	–	–	–	1.46 ± 0.55	55.83 ± 21.97
13	11:40:58.73	−26:30:22.5	2.1650	Hα	P23	5.05 ± 0.48	74.26 ± 26.26
14	11:40:37.34	−26:30:17.3	2.1684	Hα	P23	19.52 ± 6.70	6.92 ± 4.67
15	11:40:53.22	−26:30:05.4	–	–	–	9.43 ± 0.47	141.3 ± 25.8
16	11:40:52.61	−26:30:00.8	2.1577	Hα	P23	0.82 ± 0.10	38.76 ± 2.86
17	11:40:53.67	−26:30:05.8	2.1617	CO	J21	1.28 ± 0.19	56.71 ± 2.84
18	11:40:40.09	−26:29:47.4	2.1609	Hα	P23	0.72 ± 0.23	22.04 ± 5.21
19	11:40:40.11	−26:29:46.6	–	–	–	0.55 ± 0.11	26.19 ± 2.75
21	11:40:51.56	−26:29:45.7	2.1575	Hα	P23	1.06 ± 0.26	45.78 ± 12.77
22	11:40:47.46	−26:29:41.2	–	–	–	2.26 ± 0.99	35.14 ± 17.34
23	11:40:43.42	−26:29:37.3	2.1463	Hα	S14	0.51 ± 0.06	25.76 ± 1.50
24	11:40:46.86	−26:29:36.9	–	–	–	0.16 ± 0.05	6.43 ± 2.04
25	11:40:57.38	−26:29:37.5	2.1659	Hα	P23	1.26 ± 0.14	59.09 ± 2.95
26	11:40:57.64	−26:29:35.4	–	–	–	0.78 ± 0.23	27.95 ± 6.33
27	11:40:57.81	−26:29:35.7	2.1701	Hα	S14	1.90 ± 0.24	61.30 ± 4.76
28	11:40:50.70	−26:29:33.6	2.1532	CO	J21	7.61 ± 3.29	4.82 ± 4.70
29	11:40:57.91	−26:29:36.3	2.1703	Hα	P23	7.46 ± 5.65	6.18 ± 4.79
30	11:40:51.27	−26:29:38.6	2.1513	Hα	P23	8.64 ± 0.43	71.15 ± 3.56
32	11:40:43.13	−26:29:24.3	–	–	–	0.49 ± 0.07	21.07 ± 2.71
33	11:40:50.58	−26:29:21.2	–	–	–	0.46 ± 0.12	20.70 ± 3.70
34	11:40:49.81	−26:29:22.2	–	–	–	0.94 ± 0.38	36.66 ± 13.23
35	11:40:46.13	−26:29:24.7	2.1551	Hα	P23	2.06 ± 0.18	102.6 ± 5.1
36	11:40:53.72	−26:29:19.8	–	–	–	0.40 ± 0.10	17.49 ± 2.99
37	11:40:46.97	−26:29:19.2	–	–	–	1.81 ± 0.59	41.31 ± 13.43
38	11:40:50.19	−26:29:20.9	2.1543	Hα	P23	0.48 ± 0.07	24.98 ± 2.33
39	11:40:46.29	−26:29:24.3	–	–	–	5.14 ± 1.29	97.94 ± 18.64
40	11:40:44.48	−26:29:20.6	2.1620	Lyα	C05	9.19 ± 2.00	5.33 ± 3.43
41	11:40:45.77	−26:29:18.8	–	–	–	0.63 ± 0.10	29.98 ± 2.20
42	11:40:48.69	−26:29:16.4	–	–	–	0.80 ± 0.26	31.46 ± 5.16
43	11:40:36.95	−26:29:16.8	–	–	–	0.48 ± 0.06	23.79 ± 1.54
44	11:40:37.78	−26:29:12.4	2.1574	Hα	P23	4.78 ± 0.68	171.5 ± 8.6
45	11:40:48.09	−26:29:11.3	2.1415	Hα	S14	0.39 ± 0.07	13.14 ± 1.48
46	11:40:45.98	−26:29:16.7	2.1557	Hα	P23	2.10 ± 3.24	7.87 ± 7.66
48	11:40:46.67	−26:29:10.3	2.1663	Hα	P23	18.32 ± 2.16	3.53 ± 0.45
49	11:40:49.39	−26:29:09.1	2.1661	Hα	P23	0.29 ± 0.09	14.01 ± 3.01
51	11:40:44.09	−26:29:05.6	–	–	–	0.27 ± 0.15	6.78 ± 3.50
53	11:40:52.99	−26:29:04.5	–	–	–	0.67 ± 0.36	15.59 ± 9.43
54	11:40:46.07	−26:29:11.3	2.1480	Hα	S14	16.04 ± 0.80	130.3 ± 9.8
55	11:40:44.25	−26:29:07.0	2.1583	H&K	S24	23.23 ± 2.92	2.54 ± 1.23
56	11:40:48.35	−26:29:05.0	–	–	–	0.58 ± 0.30	16.69 ± 7.08
57	11:40:45.54	−26:29:02.2	2.1523	Hα	K04	0.25 ± 0.04	12.17 ± 1.05
58	11:40:47.95	−26:29:06.1	2.1568	Hα	P23	6.79 ± 1.13	41.34 ± 15.57
59	11:40:47.30	−26:28:55.5	–	–	–	0.21 ± 0.07	8.40 ± 2.52
60	11:40:41.68	−26:28:54.2	2.1634	Hα	S14	1.42 ± 0.32	62.33 ± 11.38
61	11:41:00.14	−26:28:56.3	2.1665	Hα	P23	5.27 ± 0.46	64.85 ± 10.29
62	11:41:03.28	−26:28:51.0	2.1493	Hα	P23	0.86 ± 0.26	35.74 ± 10.44
63	11:40:39.71	−26:28:49.0	–	–	–	0.31 ± 0.08	12.34 ± 2.58
64	11:40:49.49	−26:28:48.6	–	–	–	0.55 ± 0.17	22.63 ± 5.90
65	11:40:47.98	−26:28:49.6	2.1628	Hα	P23	0.92 ± 0.31	30.74 ± 7.67
66	11:40:54.81	−26:28:45.1	–	–	–	0.63 ± 0.16	23.04 ± 1.72
67	11:40:44.14	−26:28:44.0	2.1634	Hα	S14	0.48 ± 0.07	21.34 ± 2.43
68	11:40:39.73	−26:28:45.2	2.1620	Lyα	C05	14.72 ± 4.13	35.88 ± 30.98
69	11:40:51.67	−26:28:41.3	–	–	–	1.04 ± 0.29	16.54 ± 4.45
70	11:40:46.85	−26:28:41.1	2.1636	Hα	P23	0.27 ± 0.07	12.43 ± 3.29

Table A1. Continued.

ID	RA	Dec.	z_{spec}	Line	Reference	$M_\star$ (10^{10} M$_\odot$)	SFR ($M_\star$ yr^{-1})
71	11:40:55.18	−26:28:42.0	2.1630	Hα	P23	3.25 ± 1.12	3.27 ± 3.20
72	11:40:36.84	−26:28:34.1	–	–	–	0.44 ± 0.19	13.54 ± 4.83
73	11:40:48.36	−26:29:08.7	2.1618	CO	J21	261.7 ± 39.4	542.4 ± 81.1
74	11:40:44.86	−26:28:40.6	2.1435	Hα	S14	0.46 ± 0.19	15.39 ± 4.54
75	11:40:57.10	−26:28:27.9	2.1576	Hα	P23	0.87 ± 0.13	49.19 ± 4.76
76	11:40:44.75	−26:28:25.9	–	–	–	0.42 ± 0.12	14.91 ± 1.92
77	11:40:55.29	−26:28:23.8	–	Lyα	K00	3.22 ± 1.42	5.73 ± 4.23
79	11:40:56.36	−26:28:23.7	2.1892	CO	J21	0.88 ± 0.29	36.67 ± 11.72
80	11:40:54.56	−26:28:23.7	2.1606	Hα	P23	4.74 ± 0.78	185.2 ± 9.3
82	11:40:45.77	−26:28:12.5	–	–	–	3.91 ± 0.67	25.03 ± 41.57
83	11:40:45.50	−26:28:10.2	–	–	–	2.42 ± 1.11	5.85 ± 6.14
84	11:40:42.87	−26:28:07.2	2.1623	Hα	P23	0.83 ± 0.13	34.94 ± 1.93
85	11:40:36.84	−26:28:03.1	–	Lyα	K00	0.42 ± 0.10	19.55 ± 3.63
87	11:40:49.99	−26:27:54.8	–	–	–	0.19 ± 0.07	7.26 ± 1.96
88	11:41:02.44	−26:27:49.7	–	–	–	0.32 ± 0.08	12.82 ± 2.31
89	11:40:47.37	−26:27:59.1	–	–	–	4.95 ± 0.39	0.42 ± 1.77
90	11:40:55.67	−26:27:23.6	–	–	–	0.46 ± 0.20	10.83 ± 4.65
92	11:40:59.18	−26:27:56.3	2.1471	Hα	P23	0.78 ± 0.22	40.69 ± 9.80
93	11:40:54.75	−26:28:03.2	2.1516	Hα	P23	2.45 ± 1.09	73.61 ± 25.58
94	11:41:01.24	−26:27:41.7	–	–	–	0.40 ± 0.20	8.48 ± 3.50
95	11:41:02.39	−26:27:45.1	2.1510	Hα	P23	12.78 ± 16.37	65.23 ± 29.66
96	11:40:44.41	−26:27:43.0	–	–	–	0.15 ± 0.05	7.42 ± 2.16

This paper has been typeset from a TEX/LATEX file prepared by the author.